University of South Carolina
Scholar Commons

Theses and Dissertations

8-9-2014

Channel Properties of Fluvial-Tidal Transition, Santee River, SC

Kyungho Jeon
University of South Carolina - Columbia

Follow this and additional works at: https://scholarcommons.sc.edu/etd

Part of the Earth Sciences Commons

Recommended Citation

CHANNEL PROPERTIES OF FLUVIAL-TIDAL TRANSITION, SANTEE RIVER, SC

by

Kyungho Jeon

Bachelor of Science
The Pennsylvania State University – University Park, 2010

_____

Submitted in Partial Fulfillment of the Requirements

For the Degree of Master of Science in

Geological Sciences

College of Arts and Sciences

University of South Carolina

2014

Accepted by:

Raymond Torres, Director of Thesis

Alexander E. Yankovsky, Reader

L. Allan James, Reader

Lacy Ford, Vice Provost and Dean of Graduate Studies

DEDICATION

To my wife and best friend, whom I will cherish, love and lay down my life for during our lifetime together in the Messiah.

ABSTRACT

A range of studies shows that terrestrial and tidal channel dimensions increase in the downstream direction, transitioning seaward from a power function of discharge to an exponential function of distance from the coast. There are also an increasing number of studies on tidal hydrodynamics and sedimentology in channel reaches where river and tidal flows meet. However, there is a dearth of information on the channel form in fluvial-tidal transition, and therefore we have little understanding of what constitutes the fluvial-tidal transition channel, or channel reach. The Santee River in South Carolina is a gently sloping (average 10^{-5}) coastal plain river that is fully terrestrial on one side and fully tidal on the other. This thesis presents analyses of a 65-km long profile and properties of sixty-five cross sections. Fluctuations in bed elevation increase toward the mouth. Also, from the terrestrial to tidal reaches, the channel width and area increase in the downstream direction. However, further downstream channel dimensions decrease over a 30-km reach before increasing exponentially. These observations and analyses lead us to propose that there exists a geomorphic expression of the fluvial-tidal transition, and it can be detected in other river studies that illustrate similar data.

TABLE OF CONTENTS

LIST OF SYMBOLS

c   Sediment thickness

S   Sinuosity of 1km. Channel distance divided by straight line distance.

w   Width of the channel acquired by GPS

w_{image} Width of the channel acquired from plan view

A   Cross section area of flow

D   Average depth. Area divided by width.

R   Hydraulic Radius. Area divided by wetted perimeter.

a   Asymmetry of the channel cross section. The product of width and maximum depth divided by area

z   Water surface elevation

b   Exponent of the stage-area rating curve fit, $y = x^b$

x   Distance in reference to the Jamestown bridge where downstream is positive

CHAPTER 1

INTRODUCTION

Numerous studies discuss the interactions between flow processes and channel

geomorphology in rivers upstream of any tidal influence (e.g., Leopold and Maddock

1953; Schumm 1960; Leopold et al. 1964; Richards 1982; Knighton 1984; Finnegan et al.

2005). Likewise, readily available are investigations of tidal channel development (e.g.,

Langbein 1963; Wright et al. 1973) as well as sediment transport and sedimentary facies

in estuarine or tidal rivers (e.g., Allen 1991; Cattaneo and Steel 2003; Blum and

Tornqvist 2000; van den Berg et al. 2007; Dalrymple and Choi 2007). However, the

interactions between hydrodynamic processes and channel morphology where currents

transition from unidirectional downstream to bidirectional tidal are largely undocumented

(Phillips and Slattery 2007); only a handful of studies provide direct field observations

and insight on interactions between flow processes and channel geometric properties at

the intersection of the fluvial and tidal parts of the river continuum (Wright et al. 1973;

Ashley and Renwick 1983; Inokuchi 1989; Gurnell 1997; Phillips and Slattery 2007;

2008; Ensign et al. 2014). This inadequacy in focused research is noteworthy because

such information is needed to help understand ecology (e.g., Bukaveckas et al. 2011;

Ensign et al. 2012) as well as flood hazards at the upper freshwater end of the estuary,

especially in the context of sea-level rise (Florsheim et al. 2008). Presumably, this deficiency persists because of the difficulty in characterizing the highly variable fluvial-tidal hydrodynamic conditions (Yankovsky et al. 2012).

Typically, as tidal waves pass through the river mouth and advance upstream, their amplitudes increase due to channel convergence. This process leads to tidal oscillations in stage and also the onset of bidirectional flows far upstream of both the channel mouth (see the summary by Wright et al. 1973) and the zero salinity isohaline (Allen 1991). As tidal waves advance further, however, they become increasingly distorted due to bottom friction and superposition of fluvial currents (e.g., Godin 1999), this resulting in an asymptotic decline in amplitude (e.g., Jay 1991). Complete dissipation occurs far upstream of the mouth at the "tidal limit," the maximum extent of tidal effects on river systems (e.g., Wright et al. 1973; Dalrymple et al. 1992; 2007; van den Berg et al. 2007) as well as on ecosystems as well (Odum 1988). Dalrymple et al. (2012) recognized that from the mouth to the tidal limit, the channel condition shifts from tide-dominated and river-influenced to river-dominated and tide-influenced. Since discharge and tidal amplitude vary with terrestrial and marine conditions the tidal limit is a dynamic feature of the landscape. Consequently, over timescales as short as the rise and fall of a flood wave (~weeks), a lunar tide cycle (~1 month), or a variable dam release (~1 day), some channel reaches may be characterized as a "transition zone" as it links the fully fluvial to fully tidal flow conditions.

Transition zone processes have been described in facies models (e.g., van den Berg et al. 2007; Dalrymple and Choi 2007), in hydrology-energy assessments (e.g., Ensign et al. 2013, 2014), and in terms of Holocene sediment accommodation models

2

(Phillips and Slattery 2008). However, these findings are mostly presented in the context of qualitative long-term generalizations, and they do not necessarily provide the detailed insight needed for understanding channel geomorphic process-form interactions at finer temporal or spatial scales (e.g., Savenije 2005). In this sense this thesis proposes to distinguish general, long-term average conceptualizations from modern fluvial-tidal transition studies.

Much of our knowledge about modern fluvial-tidal transition geomorphology and processes comes from only a few sources. For instance, Ashley and Renwick (1983) and Ashley et al. (1988) have reported that the transition from fluvial to tidal currents and corresponding channel features occurs in a gradual manner. However, they did not sufficiently address the effects of bedrock channel and slope that are unrelated to fluvial-tidal processes. Gurnell (1997) found similar systematic channel variations in 122 cross sections along an 18-km channel reach. Regrettably, due to a downstream weir, the study site only experienced backwater effects from higher tides and no current reversals. Inokuchi (1989) examined particle size and channel properties of 466 cross sections from a 1700-km reach of the lower Mississippi River. Overall he interpreted the "inconsistencies" in sediment caliber and bed slope in the lowermost reach as a result of tidal backwater effects. Using the same data, Nittrouer et al. (2012) reported systematic variability of cross section width, depth and area at different discharge conditions and their corresponding sediment transport regimes in response to backwater effects. Yet, the study site lacked regular current reversals, which may occur only during hurricane events (Demas 2012). Wright et al. (1973) studied channel development in the funnel-shaped Ord River system. Their work related tidal distortion and tidal wavelength to channel

Figure 1.1 US southeastern coastal plain and the rivers that flow through it. The Santee River is denoted with a black cross, centering near the Hwy-Alt 17 Bridge near Jamestown. Modified from Campbell et al. (2011).

properties expressed through equilibrium between tidal prism and equal work per unit bed area that gives rise to a distinct channel form. Phillips and Slattery (2007) highlighted the role of topography and antecedent landforms in sediment bottlenecks upstream of the modern fluvial-tidal transition. Further downstream, however, they report that channel slope and stream power decrease systematically (see also Ensign et al. 2013).

One interesting facet of these studies is that most are about rivers that traverse a coastal plain, whereas the conceptual models presented above, which describe transition zone processes, forms and sedimentary facies, have been developed almost exclusively for submerged river valleys and strongly converging funnel-shaped estuaries (e.g., Dalrymple and Choi 2007). Yet, the U.S. coastal plain consists not only of drowned river valleys but also of other estuarine variants depending on various tidal and sedimentary regimes. For instance, Ensign et al. (2013, 2014) conducted hydrologic-tidal studies in coastal plain rivers that lack submerged river valleys. How coastal plain rivers of various types translate to processes, channel forms and facies has not been fully explored.

The purpose of this thesis is to investigate channel forms of the reach that links fully fluvial and fully tidal conditions in the upper alluvial estuary. It endeavors to improve on the characterization of fluvial-tidal transitions by observing channel morphology in the Santee River—a coastal plain, tide-affected river (Figure 1.1). This work will highlight a part of the geomorphic river continuum for which few measurements exist. As Figure 1.1 shows, findings from this study will be applicable to all rivers along the U.S. coastal plain from Texas to New Jersey. Moreover, given the highly dynamic nature of the transition zone, it is likely that both process and form

respond over timescales commensurate with climate change and sea-level rise. Hence,

detailed observations and analyses of modern transition zones will, for example, help

with low-elevation land-use planning. Such investigations will help shed light on a

poorly documented component of the fluvial landscape, and they will help support the

utility of generalized facies models that are taken to represent average conditions over

much longer timescales (e.g., Blum and Torqvist 2000, Cattaneo and Steel 2003;

Dalrymple and Choi 2007). Furthermore, this thesis will highlight the relationships

between dependent and independent variables in landscape morphodynamics that vary

with the timescales under consideration (Schumm and Lichty 1965). This study focuses

on a modern coastal plain freshwater river reach where the channel flow shows current

reversals during low discharges and backwater effects during high discharges. Here we

ask the question: Are there channel features intrinsic to the fluvial-tidal transition?

CHAPTER 2

STUDY SITE

The Santee River watershed has a drainage area of ~40,000 km^2 covering North and South Carolina, with its headwaters starting in the Blue Ridge and the Piedmont (Hughes 1994). The drainage basin constitutes one of the largest river systems in the eastern U.S. (Eckard 1983). The Santee River is located in the U.S. southeast coastal plain, this implying the potential applicability of this study to the majority of the tidal river systems illustrated in Figure 1.1.

The Santee River forms as the Wateree and the Congaree Rivers merge, and flows ~230 km through the coastal plain of South Carolina and out to its deltaic mouth ~24 km south of Georgetown, SC. Downstream from the confluence, the Lakes Marion and Moultrie were formed in 1941 with the construction of dams for hydroelectric power. The flow had been diverted to the Cooper River temporarily and was subsequently rerouted to the Santee River (Kjerfve and Greer 1978; Hodge 1981).

The mean annual discharge of the Santee River from 1987 to 2005 was ~311 m^3/s, flushing 0.86 megatons of sediment (Milliman and Farnsworth 2005). USGS maintains a real-time gaging station ~2 km northeast of Jamestown (#02171700, 33.18° N, 79.40°W, 2.42 m at NAVD88) that records the current velocity (using a SonTek Argonaut SL) and water stage (using a wire weight gage). The recorded maximum discharge is

2,888 m^3/s (Mar 28, 2003) and the minimum, –67.7 m^3/s (Oct 24, 2008). The maximum

and minimum discharge records for the study year 2013 were 1,537.6 m^3/s (Jul 20) and

–40.8 m^3/s (Nov 14), respectively. The NGS tidal datum at the Jamestown bridge is at

0.33 m (NAVD88) with Mean High Water 0.50 m, Mean Sea Level 0.31 m and Mean

Low Water 0.16 m. Tide range at the mouth and adjacent inlets is 1.16 m (NAVD88),

with MHW 0.54 m, MSL –0.05 m and MLW at 0.63 m (See also Yankovsky et al. 2012).

The ~65-km survey reach is between ~95 km and 35 km upstream from the mouth.

The channel planform is mostly sinuous, with interment <5 km-long straighter reaches

(Figure 2.1). The best-developed meanders are near the distributary bifurcations. There

are 7 tributaries along the study reach but they are relatively small, with mouth width < 6

m, and the drainage area is limited to the adjacent and typically flat-lying floodplain. Our

geomorphic analyses end at the distributary bifurcation of the North and South Santee

rivers near Goat Island (Figure 2.1). However, there is one smaller distributary channel

in the study reach that is 7-m wide at the mouth and connects to the North Santee River

downstream of our survey.

The study reach can be characterized as freshwater tidal, knowing that the 1ppt

salinity isohaline is found 8 km upriver from the mouth during low discharge conditions

(Kjerfve and Greer 1978). The Jamestown bridge was selected as the reference frame for

distance due primarily to its tidal signals at low discharge conditions and to the absence

of another objective physical basis for reference in the vicinity (Figure 1.1). In reference

to the bridge, positive distance is in the downstream direction, and thus our study reach

spanned from −35 km to +30 km. Henceforth, locations are reported as km-distance from

the bridge.

Figure 2.1 The span of the ~65-km study site. The upper and lower limits are marked by white blocks. The USGS gaging station is at 0 km. Downstream is to the right.

The underlying bedrock in the study zone is Eocene Santee Limestone generally striking north/northeast and gently dipping south/southeast (Siple 1960). Also limestone sinkholes are found commonly around the town of Santee, and based on air photo interpretation they may exist near the study reach. However, limestone exposures are confined to the left bank of a straight portion of the channel, and the majority of the channel banks and floodplains consists of clay and silt.

The bed sediment thickness, c, along a 20.1-km extent, ranged from 0 m to 3m at distinctly bedrock reaches that lack sediment (Figure 2.2, Walker 2011). For example, thick c is found in the upper section from −6 km to −2 km and from +7 km to +14 km. However, from −1 km to +7 km the value is ~0 m for the most part. The $c > 0$ m occurs sporadically throughout the −6 km to +14 km, but thickest sediment $c > 2$ m occurs at −5.5 km, −3 km, −2.5 km, from 2 km to +3 km and at +13.5 km.

The reach of $c > 0$ m constitutes ~12.6 km (~63%) of the total length. The remaining ~7.5 km (~37%) lacks sediment and is thus identified as bedrock sections (Figure 2.2). From −6 km to +14 km the thickness ranges between 0 m and 3.4 m. From −6 km to −1 km the average thickness is 1.3 m±0.8 m, fluctuating between 0 m and 3 m though 0 m rarely occurs. From −1 km to +7 km the thickness ranges from 0 m to 1 m (mean 0.3 m± 0.5 m) with the section of bank outcrop from +2 km to +7 km. In the downstream from +7 km to +14 km, c fluctuates between 0 m and 1.5 m. Bedrock seems to appear intermittently in this section though the mean sediment thickness remains higher at 0.6 m±0.7 m; no bank exposure was observed in the field. The rock outcrop observed in the field from +2 km to +7 km will henceforth be cited as the bedrock section.
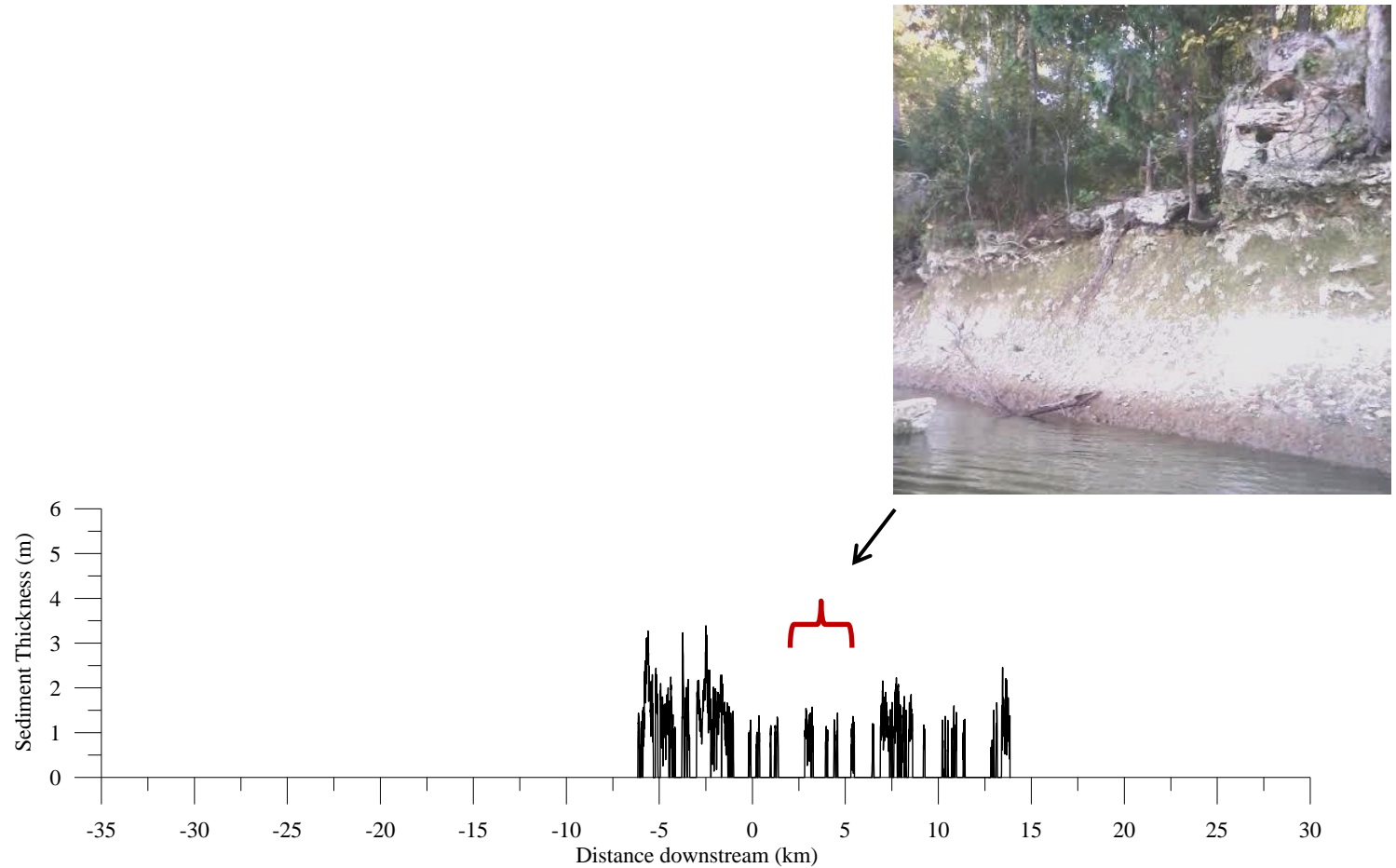
Figure 2.2 Sediment thickness (*c*) with distance (*x*) and a field photo of the bank rock outcrop. The survey reach by Walker (2011) spanned from -6 km to +14 km. The photo, taken at the bedrock section indicated by the red bracket, views the bank from its first appearance at +2 km in the downstream direction until ~7 km.

CHAPTER 3

METHODS

3.1 Equipment and settings

A Trimble R8 GPS system and the Seafloor SonarMite (Hydrolite-TM) echo sounder were installed on a johnboat (average speed maintained at ~2 m/s) to acquire the *xyz*-positions of the sounder (positioned ~0.1 m below the water surface) and distance to the river bed, respectively. The South Carolina GPS Virtual Reference Station (VRS) through the cellular wireless Internet connection served as the base station for a Real Time Kinematic survey (Lapine and Wellslager 2007). The GPS has an accuracy of 10mm+1ppm RMS horizontally and of 20 mm+1 ppm RMS vertically for static surveys (for every km added to the distance between the GPS and base station, 0.5 mm of given error is added). The "Continuous Topo" mode was used, which lowers the accuracy 2–3 times as the frequency of sampling is raised to 2–3 Hz. The echo sounder transducer pings at 6 Hz (wave frequency: 235 kHz), and its accuracy is <10 mm (or 0.1% of depth), with a measurement capacity ranging from 0.3 m to 75 m. The VRS-GPS and echo sounder were integrated with a Trimble survey controller TSC2 via wireless and Blue Tooth connection. The Wilson Electronic Sleek Wireless Signal Booster was used to augment the Internet connection.

All field survey data were referenced to UTM (Universal Transverse Mercator, 17 North) for the horizontal and NAVD88 (North American Vertical Datum of 1988) for the vertical. The USGS gaging station is at 2.42 m in NAVD88 (water surface was read for 5 minutes with our equipment to reference the station to this vertical datum). Surveys took place, on Mar 11–12, Aug 31, Nov 17, and Dec 20–21 in 2013. The following are the stage and discharge records from the gaging station during our surveys referenced to NAVD88. On Mar 11–12, the water stage ranged between –0.82 m and –0.77 m, and between –0.29 m and –0.26 m. The corresponding discharges were 109.6 m^3/s to154.0 m^3/s and 227.1 m^3/s to 235.9 m^3/s, respectively. On Aug 31 the stage and discharge were 1.27 m to 1.39 m and 433.3 m^3/s to 441.7 m^3/s, respectively. On Nov 17 stage and discharge were –0.9m to –0.77 m and 133.9 m^3/s to 163.7 m^3/s, respectively. On Dec 20–21 the stages were 0.26 m to 0.27 m and 0.32 m to 0.37 m. The respective discharges were 348.3 m^3/s to 359.6 m^3/s.

3.2 Channel geometry data

3.2.1 Plan-view survey of width and sinuosity

Channel width was estimated by using Google Earth. The canopy-to-canopy width was measured at 1-km intervals along the channel overlapping the field survey reach. Full channel width was measured by selecting the nearest point without tree canopy or assuming ~5 m for the channel bank under the canopy. The Santee River bifurcates into the North and the South Santee Rivers ~30 km downriver from the bridge; the widths of the distributaries were summed. Sinuosity was also measured by using Google Earth at each transect. The 1-km river distance and corresponding straight line

distance was represented as a ratio value of river distance to straight line distance. Sinuosity values of 1.0 were the straight channel reaches (e.g., Leopold et al. 1964).

3.2.2 Riverbed long profile

The long profile was surveyed at a 5-m interval with the boat course maintained in the middle of the river at straight sections and ~30% closer to the outer bank at bends. This survey took place on two separate occasions covering the lower and the upper reaches (Mar 11–12 and Nov 17, 2013). The two survey zones of the long profile overlapped by ~3 km, which enabled the two datasets to be linked. The combined data set spanned ~65 km. The riverbed elevation values were acquired by subtracting the echo sounder depths from the water surface elevations (NAVD88). To assure that the long profile dataset kept the general trends and omitted missing points, the data were interpolated using a Matlab script with 5-m equidistance data. Also, general statistics were acquired over a running 5-km window.

3.2.3 Cross section transects

Sixty-five cross section profiles were surveyed perpendicular to the flow between the ~65 km river distance covered by long profile survey (on Aug 30, Nov 17 and Dec 20–21, 2013). The transects were spaced at ~1 km. In some cases, maintaining a survey transect that is perpendicular to the flow direction was problematic, especially at reaches with strong currents. When this occurred, the cross sections were attempted multiple times to obtain points within 5 m of the straight line across the channel, estimated in the plan view with the Esri-ArcGIS. For each across-channel survey, or transect, the analysis

employed a Matlab script for orthogonal projection, collapsing the points within 5 m of the transect line onto a single straight line across the channel.

In most cases the tree canopy caused disconnection to the VRS. Sometimes this problem could be addressed by boating to the mid-channel to regain the signal and quickly finishing the survey of the bank segment before disconnection. At times this approach allowed data points to be collected within 1 m of the banks. In other cases when GPS surveying was not possible under the canopy, the distance from the last survey point to the water edge as well as the slope of the channel bank were estimated, and the profiles were adjusted accordingly.

In order to estimate channel properties that correspond to a single discharge value, it was necessary to adjust the water level data between surveys. In such instances, the higher discharge was decreased to the lower discharge, to approximately the bankfull discharge. The water stage was lowered to the Nov 17 conditions, which showed a minor stage decrease (~0.30 m) at the USGS gaging station. The stage throughout the Nov 17 survey reach (~16.1 km) gave the slope -6.82×10^{-5}. This slope was applied to the surveys of higher water stages. The resulting water level projection was reliable given that overlapping cross-channel and along-channel surveys from different stage conditions yielded similar area estimates.

Cross section data were analyzed with the freeware WinXSPro from the US Forest Service (e.g., Cornwell et al. 2003; Sandercock and Hooke 2010). The program requires channel cross section data, and it computes width, mean depth, cross section area, wetted perimeter (the "wetted" cross channel boundary distance) and hydraulic radius (cross section area of flow divided by wetted perimeter). Area estimates employ

Simpson's method of integration, which calculates the area under the water surface (Hardy et al., 2005). The program computes the area at 0.01-m stage increments up to the desired stage level. Hence, cross section area was also acquired as a function of stage height, or rating curves, for the flow stage at the time of the field survey.

3.2.4 Channel cross section shape analysis

Dimensionless stage-area rating curves were analyzed to characterize the cross section shapes. Based on how much stage increment is needed from the channel bottom to top, the curve of the stage-area trend changes. If area increases more per stage increment, the channel depth across is relatively uniform; if area increases less per stage interval, the channel depth is relatively irregular.

A dimensionless stage-area curve for a cross section consists of the ratios of stage to maximum stage versus area to maximum area. The dimensionless values allow comparison of channel cross section shapes irrespective of channel size. Exponential curves were fits to the dimensionless stage-area plots using CurveExpert Professional software:

$$\mathbf{y = ax^b}$$

where **y** is area/area(max) and **x** is stage/stage(max) with the coefficient **a** fixed at 1.0. Though stage on the **y**-axis is intuitive and commonplace (e.g., Leopold et al. 1964), here the output is an exponential function that allows the exponent to be an integer as opposed to a power function, which would yield a decimal.

CHAPTER 4

RESULTS

4.1 Long profile

4.1.1 Bed elevation

Overall, the 65-km riverbed profile elevation declines ~5 m in the downstream

direction, and the average slope of linear regression is $-5.74\text{x}10^{-5}$ (R^2=0.48). However,

the decline is highly irregular (Figure 4.1A). For instance, the downstream reach that

extends from +7 km to +32 km has much larger and much more frequently occurring

depressions or "deeps" that are 2 m to 8 m lower than the background bed elevation. The

largest of these depressions are at +8 km and +32 km, and extend for several kilometers.

The upstream reach has typically smaller fluctuations with the exception of a 6-km reach

from −18 km to −12 km. Otherwise, the fluctuations from −34 km to +2 km are < 2 m,

and they appear more frequently. Also, the slopes between upstream and downstream

differ substantially. The linear regression fit from the upstream limit to −5 km is

$-9.05\text{x}10^{-2}$ (R^2=0.43). The downstream slope from +5 km to the downstream limit is

$-6.6\text{x}10^{-2}$ (R^2=0.24). On the other hand, there are sections of the channel that have

very slight fluctuations in bed elevation (< 1 m). For example, at +3 km there is a 4-km

reach of relatively smooth bed. This section coincides with bedrock exposures on the
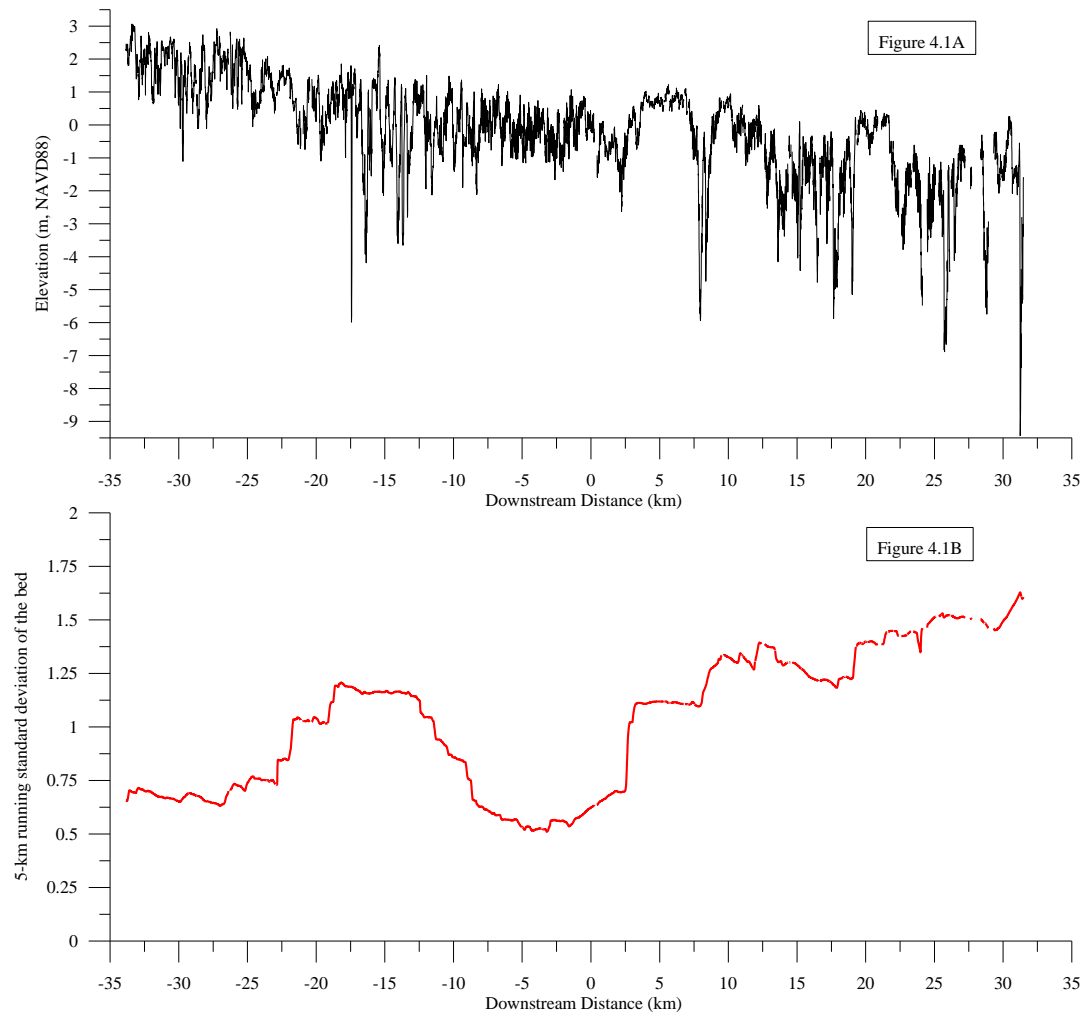
Figure 4.1 A and 4.1 B Long profile of the riverbed (Figure 4.1 A), and the 5-km moving standard deviation of the riverbed elevation (4.1 B). The 5-km running standard deviation is shown in red indicates the intensity of riverbed fluctuations.

bank, which likely reflects the occurrence of a bedrock channel (Walker 2011). This location is accompanied by the break in slope between upstream and downstream reaches. Two other reaches have a similar appearance, but their cause is not as clear because bedrock was not found at either location (from +9 km to +10 km and from +18 km to +22 km). The mean elevation for the upstream reach from −35 km to +2.5 km is 0.5 m±0.8 m and in the downstream from +2.5 km to +32 km is −1.1 m±1.3 m. The mean bed elevation at the rock outcrop around +5 km is 0.4 m±0.5 m and corresponds to its flat top with the least amount of fluctuation.

These trends in bed elevation are also apparent in the standard deviation of mean bed elevation assessed over a 5-km window. This analysis shows an overall ~1 m increase in the downstream direction (Figure 4.1B). The upstream reach shows a relatively low and consistent standard deviation of 0.7 m except for the local increase associated with the deeps between −25 km and −7.5 km. These fluctuations give a peak value of 1.2 m. Therefore, we characterize the upstream reach as having a local high amount of fluctuation surrounded by a much smoother reach. At +2.5 km there is a step-like increase and a relatively smooth decrease that correspond to the start of the rock outcrop reach described above; from +2 km to +7 km the values remain nearly constant at 1.2 m. Thereafter, the standard deviation consistently increases to the end of the survey reach.

4.1.2 Thalweg elevation

The 65 thalweg values, the lowest elevation in each cross section, decrease ~7 m from +2.5 m to −6.5 m in the downstream direction in a non-uniform fashion (Figure 4.2).

19
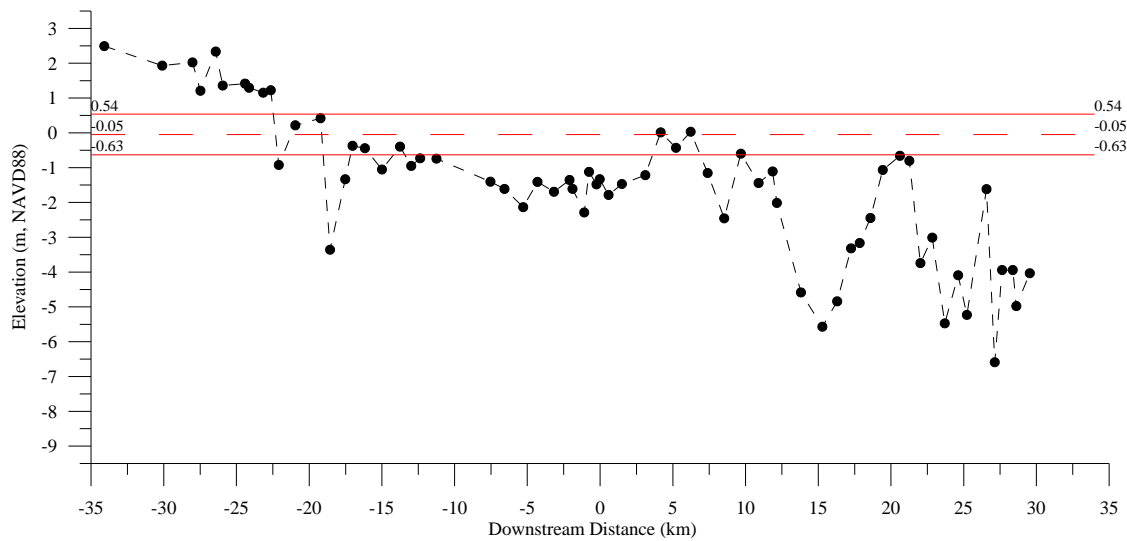
Figure 4.2 Thalweg and tidal elevations. Note the decrease of the bed elevation from ~3 m to ~ −9 m in the downstream direction. The thalweg elevation decreases in the more upstream region and fluctuates more in the downstream. The red lines are tidal elevations: MHW (0.54 m), MSL (-0.05 m) and MLW (-0.63 m).

In particular, these variations mimic those from the more frequently measured long profile elevations. Many discrepancies, however, occur between the profile and thalweg elevations, which is most likely due to the boat not traveling consistently along the deepest part of the channel. Also, as with the long profile data, the thalweg profile shows strong difference between upstream and downstream trends. For example, the upstream reach is characterized by a uniform decline of ~4 m from −34 km to −5 km, with a linear regression slope of $−1.66 \times 10^{−1}$ (R^2=0.68). From −5 km to +3 km the values vary slightly (<1 m). At +4 km there is an abrupt increase followed by an overall decreasing trend with 5–6 m fluctuations. The rock outcrop reach is represented by the locally high thalweg values of about 0 m from +2 km to +7 km. The mean slope from +5 km to the downstream limit is $−1.48 \times 10^{−1}$ (R^2=0.35).

Tidal elevations based on data from the mouth are displayed in Figure 4.2 as horizontal lines in order to facilitate comparison with thalweg elevations. The tidal elevations that were used include mean high water (MHW), mean sea level (MSL) and mean low water (MLW), corresponding to 0.54 m, −0.05 m and −0.63 m, respectively. As opposed to the full long profile (Figure 4.1A), Figure 4.2 compares tidal elevations to thalweg data for two reasons. First, the river bottom can be considered as a type of boundary to tidal effects. Second, the long profile survey was not necessarily over the thalweg. Overall, the profile spans all three tidal elevations. From −34 km to −22 km the thalweg is higher than MHW, and from −21 km to −15 km, most values are between MHW and MLW, as are the thalweg elevations of the bedrock reach (+2 km to +7 km). From −13 km to +30 km, all but 4 values are below MLW. Hence, the thalweg profile spans all three tidal elevations, but most of the channel is below MLW. These

observations indicate that most if not all of the channel, up to 100 km inland, is influenced by tidal variations in velocity and stage.

4.1.3 Sinuosity(S)

The 65-km channel reach can be characterized as straight with mostly low amplitude meanders. The largest and best-developed meanders occur near the downstream end of the survey (Figure 4.3). At this location there are two meanders with an amplitude and wavelength of ~1 km. Upstream to ~6 km past the bridge the channel is mostly straight except for one tight set of bends midway at ~ +14 km. Further upstream the channel transitions to a mostly sinuous planform with meanders having amplitudes of 0.3 km to 0.6 km and wavelengths up to 2.2 km. *S* values range from 1.0 to 3.1, with an average of 1.21±0.39. Therefore, the entire reach can be characterized as being relatively straight with low amplitude bends. Moreover, because each *S* value was computed along a 1-km sample reach, the peaked nature of the sinuosity plot (Figure 4.3) indicates that wavelengths of the bends are likely < 2 km.

Nearly 80% of the *S* values are < 1.3, and many instances of 1.0<*S*<1.1 occur over the entire reach. In particular, from −35 km to −2 km, the mean is 1.27±0.42. From −2 km to +13 km, the mean *S* is 1.01±0.02. This reach includes the bedrock section. However, from +13 km to +30 km *S* becomes highly variable with an average of 1.28±0.42. Figure 4.3 highlights the variability in *S*. The values >1.4 coincide with the downstream meanders and two sites upstream, where there are intermittent tight bends. Also, along the survey reach the *S*>1.4 occurrences give rise to single-value peaks along channel (Figure 4.3) at, for instance, −17 km, −6 km, +13 km and from +23 km to +27
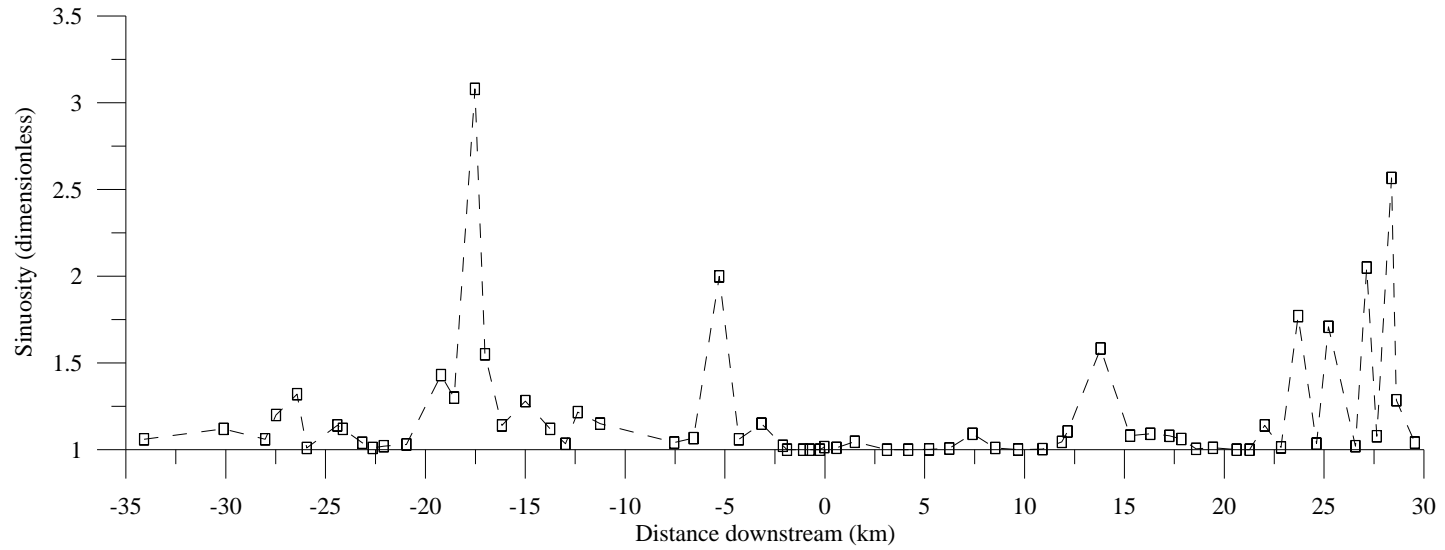
Figure 4.3 Sinuosity (1km) downstream. About 80% of the values are <1.3, and peaks above 1.43 occur throughout, though low sinuosity (1.01±0.02) dominates from −2 km to +22 km (excluding from +12.5 km to +15 km).

km. Moreover, the deeper parts of the upstream reach of the long profile (Figure 4.1A), at –20 km to –15 km, coincide with some of the larger S values in that region. Hence, the aberrant deep sections of the river in the upstream reach appear to be associated with the larger meanders.

4.1.4 Summary

The 65-km channel thalweg is mostly below MLW. Nevertheless, based on slope and variations in bed elevation, the channel can be divided into upstream and downstream zones. In the upstream the river bed is relatively smoother than the downstream. Also, the average slopes differ substantially with the upstream being much steeper. The break in slope between upstream and downstream is associated with the occurrence of a 5-km reach of bedrock channel.

4.2 Cross section properties

The following presents a one-dimensional assessment of variables that were measured directly in the field or that were computed from field observations. There follows a spatial assessment (4.3) that highlights how these variables change along the channel, and identifies patterns of variation that may be associated with the fluvial-tidal transition.

4.2.1 Width (w_i and w)

The w_i refers to the channel width measured from Google Earth. The w_i value was measured every 1 km from the mouth to 95 km upstream (Figure 4.4A). Widths

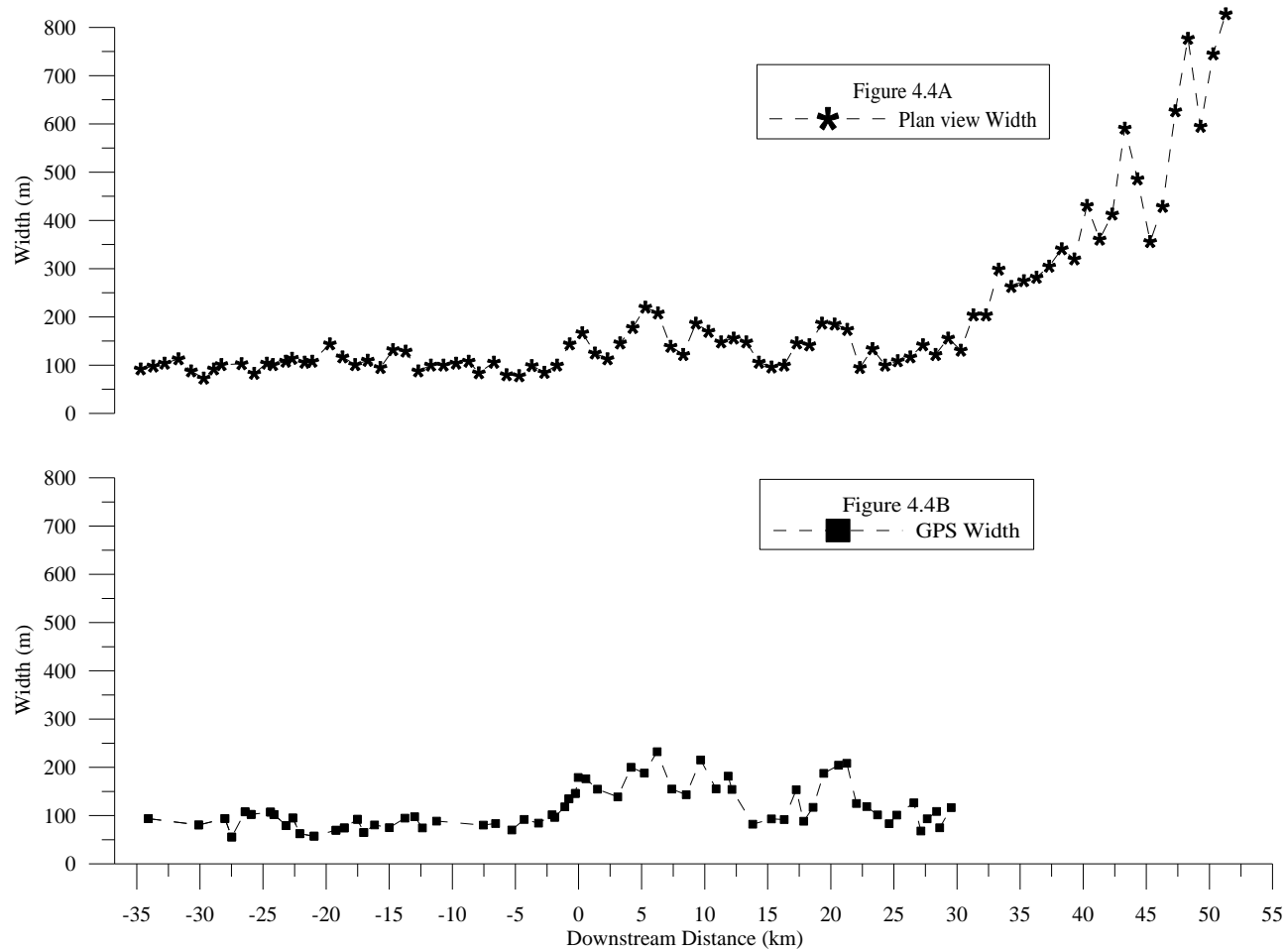Figure 4.4A and B Plan view width (w_{image}) and GPS width (w) in the downstream distance (x). The w_{image} includes the extent +30 km to +55 km, which is downstream from the bifurcated distributaries—the North and the South Santee Rivers. The lower plot is the field survey width extends from –35 km to +30 km. Note the close pattern in the local highs from 0 km to +13 km and from +19 km to +22 km.

ranged from 73 m to 828 m and averaged 197 m±164 m. Nearly 80% of the values were

upstream of the North and South Santee bifurcation and were typically <250 m. Roughly

~10% of the values were >590 m and occurred closer to the coast. Because of its highly

skewed distribution (2.26), >76% of the values were outside the 95% confidence interval.

Width increases at a very low rate per kilometer in the downstream direction

(Figure 4.4A), from −34 km to +30 km. Further downstream, width increases at a much

greater rate, with 7–8 fold increase over ~ 25 km, giving rise to the typical exponential

increase with distance downstream. The function that best describes the increasing trend

of w_i is $29.4e^{0.5x}$ (R^2=0.87). Moreover, there are only three locations along the channel

that appear to depart from the expected values. These areas are centered at +7 km, +20

km and +47 km (Figure 4.4A).

The survey widths were taken from −35 km to +30 km, where the image-based

width (w_i) begins to increase rapidly (Figure 4.4B). The w values range from 56 m to

232 m and average 115 m±44 m. Notably the values ranging from 176 m to 204 m are

outside the 95% confidence interval, this indicating the skewed or exponential

distribution. Also, these larger values are found in the middle of the surveyed length,

unlike the highest w_i values, which occur near the mouth. A linear trend of w_i and w has a

slope of 1.12 (R^2=0.85). In the overlapping section upstream from the distributaries, the

positions of minimum and maximum between data sets nearly overlap as well.

4.2.2 Average depth (D) and hydraulic radius (R)

Water depth was highly variable due in part to variations in discharge but more

importantly to the large fluctuations in bed elevation, as described above. During the

surveys, the higher water depths were 8 m to 12 m. On the other hand, average depth, D, was less variable. Average depth was computed by dividing the cross section area by the surveyed width. Average depth ranges from 1.27 m to 4.50 m, with a mean of 2.64 m±0.80 m; only the lowest value 1.27 m is outside the 95% confidence interval. Most values are <3.5 m, and the two highest values, 4.50 m and 4.31 m, occur at −22 km and +14 km, respectively.

The hydraulic radius, R, is taken as the cross section area divided by the wetted perimeter. R values are typically interpreted as a type of "river efficiency parameter" because it represents an estimate of the water-solid contact area. The values of R range from 1.25 m to 4.14 m, with a mean of 2.53 m±0.65 m. The minimum R, or less efficient channel, occurs in the downstream at +19 km, whereas the maximum or most efficient channel occurs at +14 km. All values are within the 95% confidence interval. Fewer than 10% of the values are >3.5 m.

In addition to an efficiency parameter, R is comparable to average depth, D. A plot of D versus R shows a strong positive linear correlation at 0.81 (R^2=0.93) but with D greater than R at deeper depths (Figure 4.5). The correlation is strongest up to 3m. Subsequently, the data fall below the 1:1 line, meaning that for values > 3m the R underestimates D. This trend is likely due to greater wetted perimeters associated with the larger channels. Therefore, larger channels seem to have more irregular bottom profiles.

4.2.3 w:d, and w:R

The ratio of width to depth, *w:d*, provides some insight into channel shape. Based
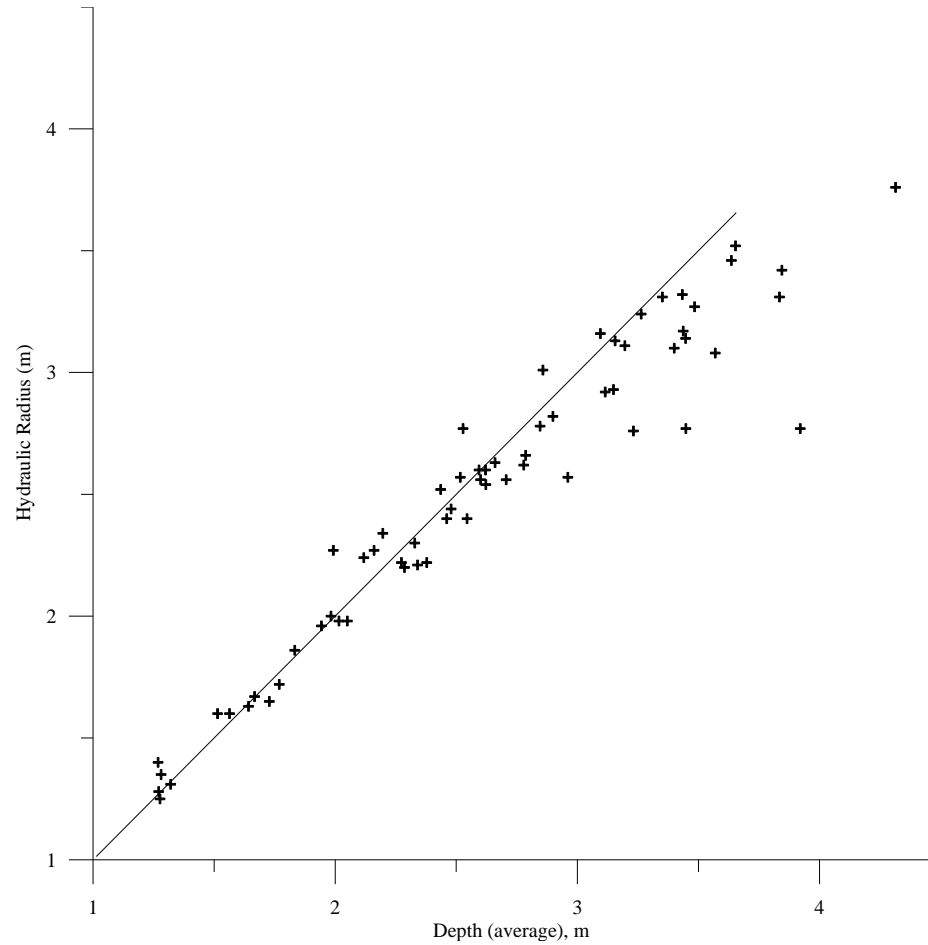
27

Figure 4.5 Average depth (*D*) versus hydraulic radius (*R*). The straight line is 1:1 ratio, which shows that the higher values are slanted toward average depth. From the lowest values to ~3 m, the parameters are more closely distributed, yet from ~3 m to ~4.5 m there is a skew toward *D*. A close positive linear correlation exists, however, between *D* and *R* at 0.81 (R^2=0.93).

on observations in the field, the channel is typically much wider than it is deep. This is apparent in the high and highly variable *w:d* ratios, with a range from 14.4 to 163.0 and a mean of 52.4±38.0. Although there are no statistical outliers, only 24 values or 36% of the observations are within the 95% confidence limits.

The slope of the line relating width and depth for a series of observations along a channel can provide an estimate for a population-averaged *w:d* ratio (e.g., Finnegan et al. 2005). Here we plot *w* versus *R*, with *R* taken as a proxy for depth because the *D* values reported here were computed as area/width, whereas *R* represents area/wetted perimeter. The *w* versus *R* relationship is characterized by a weak and negative association (Figure 4.6), with R^2=0.33 and slope = -8.68×10^{-3}, respectively. The largest scatter occurs over *w* range of 56 m to 100 m. The scatter, however, declines with increasing width, perhaps because there are fewer points. This *w-R* trend indicates that the "average" *w:R* ~ 38.4. Two points about this value, first the absolute value 38, is in the range of the *w:d* values measured directly. Second, the negative slope of the relationships is in contrast to similar analyses applied to terrestrial rivers with a positive association (e.g., Finnegan et al. 2005). Therefore, given the earlier observation that width is increasing slightly in the downstream direction (Figures 4.4A, 4.4B), maintaining the *w:R* population average of 38 requires that channel *R* (~depth) also increase slightly.

4.2.4 Cross section area (A) and profile shape

The cross section area *A* ranges from 118 m^2 to 553 m^2 and averages 282 m^2±82 m^2. The minimum 118 m^2 is found at the upstream limit, whereas the maximum 553 m^2, an outlier, occurs in the middle of the survey reach (~ 0 km). Moreover, the channel
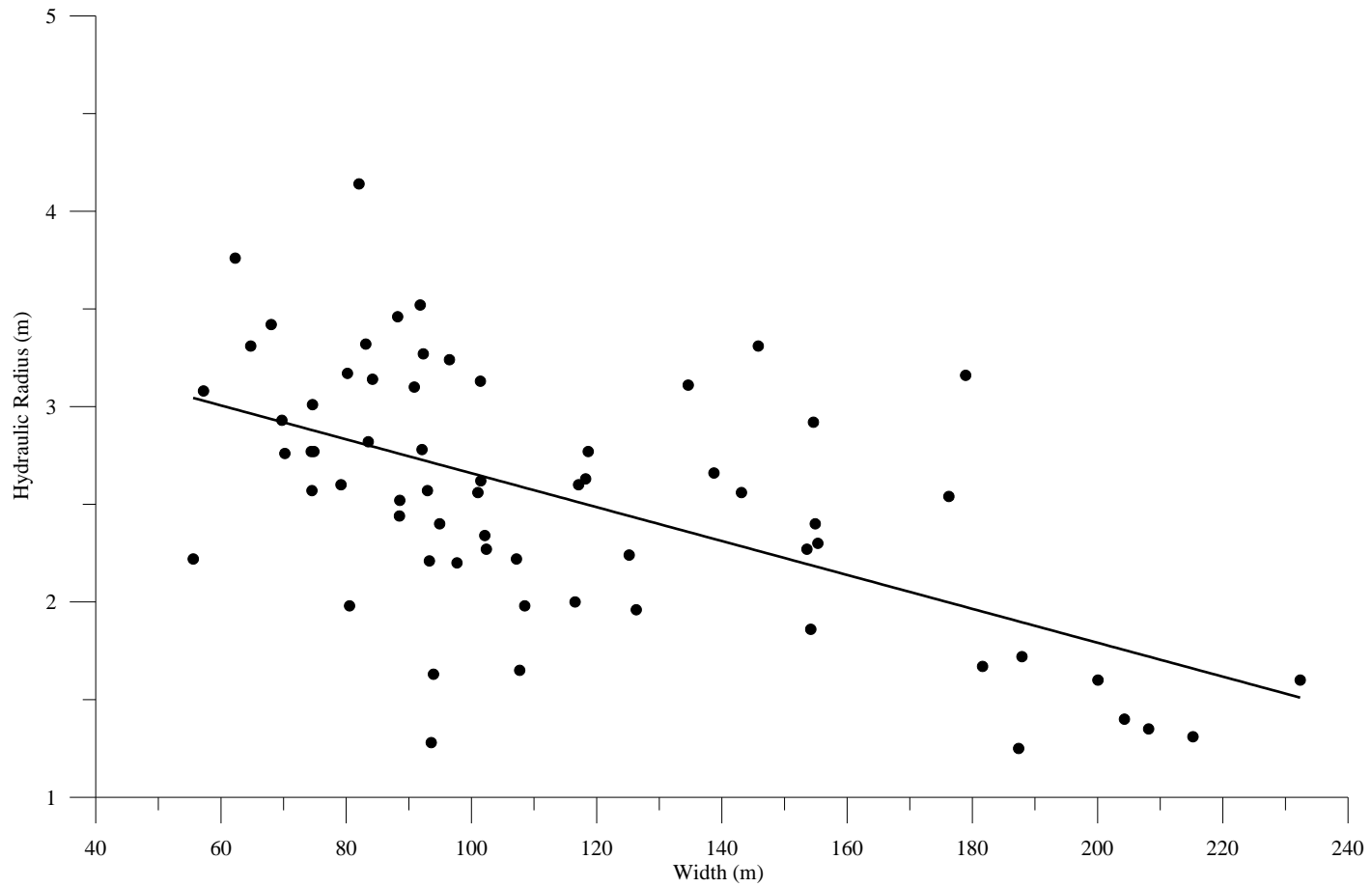
Figure 4.6 Width (w) versus hydraulic radius (R). With high hydraulic radius, width is low; and width low hydraulic radius, width high. The slope is -8.68×10^{-3} (R^2=0.33).

cross sections with the five highest areas (from 430 m^2 to 488 m^2) are all proximal to each other. Hence, there is a ~5 km reach that has the greatest cross sectional area values of the entire survey. Also, these five values are outside of the 95% confidence limit.

By precluding the vertical exaggeration from plots of the cross section bed elevation versus distance across, it is clear that the width is substantially greater than depth (Figure 4.7). Three main channel types were identified from the range of cross sections evaluated. The "uniform" channel is characterized by relatively uniform channel depth with gradual banks (Figure 4.7A). Departure from the uniform channel gives rise to increasing variability in depth and bank steepness. Therefore, the "trapezoidal" channel has a slightly varying depth with steeper bank (Figure 4.7B), and the third, the "irregular" channel, is narrower, has a depth of at least 7 m, and features at least one vertical bank (Figure 4.7C).

Values of cross section asymmetry, taken as the product of width and maximum depth divided by area, range from 1.14 to 2.33 with an average of 1.45±0.26. About 12% of these values lie outside the 95% confidence limits. Of these, the five lowest (from 1.14 to 1.17) occur in the upstream, whereas the three largest (from 2.0 to 2.33) are found in the downstream. Moreover, 80% of the asymmetry values range from 1.14 to 1.64, which indicates that the majority of the cross sections are nearly symmetrical. Both the minimum and maximum values occur in the upstream reach.

Each channel cross section size and shape can be represented by a line (ranging from straight to curved) that relates water stage to cross section area of flow, *A* vs *z*, often cited as a "rating curve" (Figure 4.8). For the wide and shallow Santee River cross sections, the curves increase from the origin at a relatively lower rate, but the rate (slope)

31
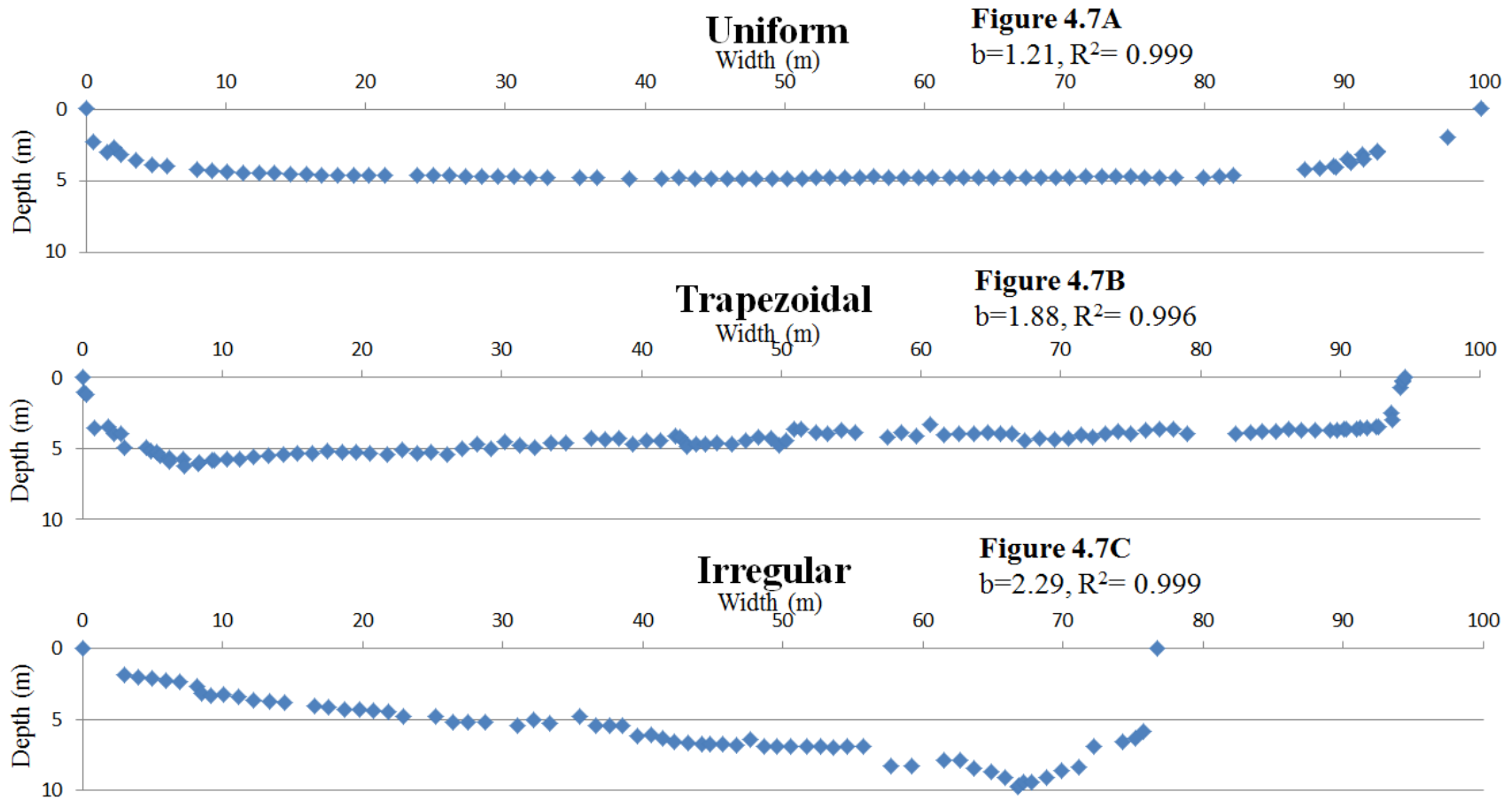
Figure 4.7A, B and C. The three main cross section channel shapes. From uniform to irregular the channel depth across becomes uneven as it deviates from uniform. Trapezoidal is the intermediate shape. The curve-fit exponent *b* and correlation coefficient is given for each example.
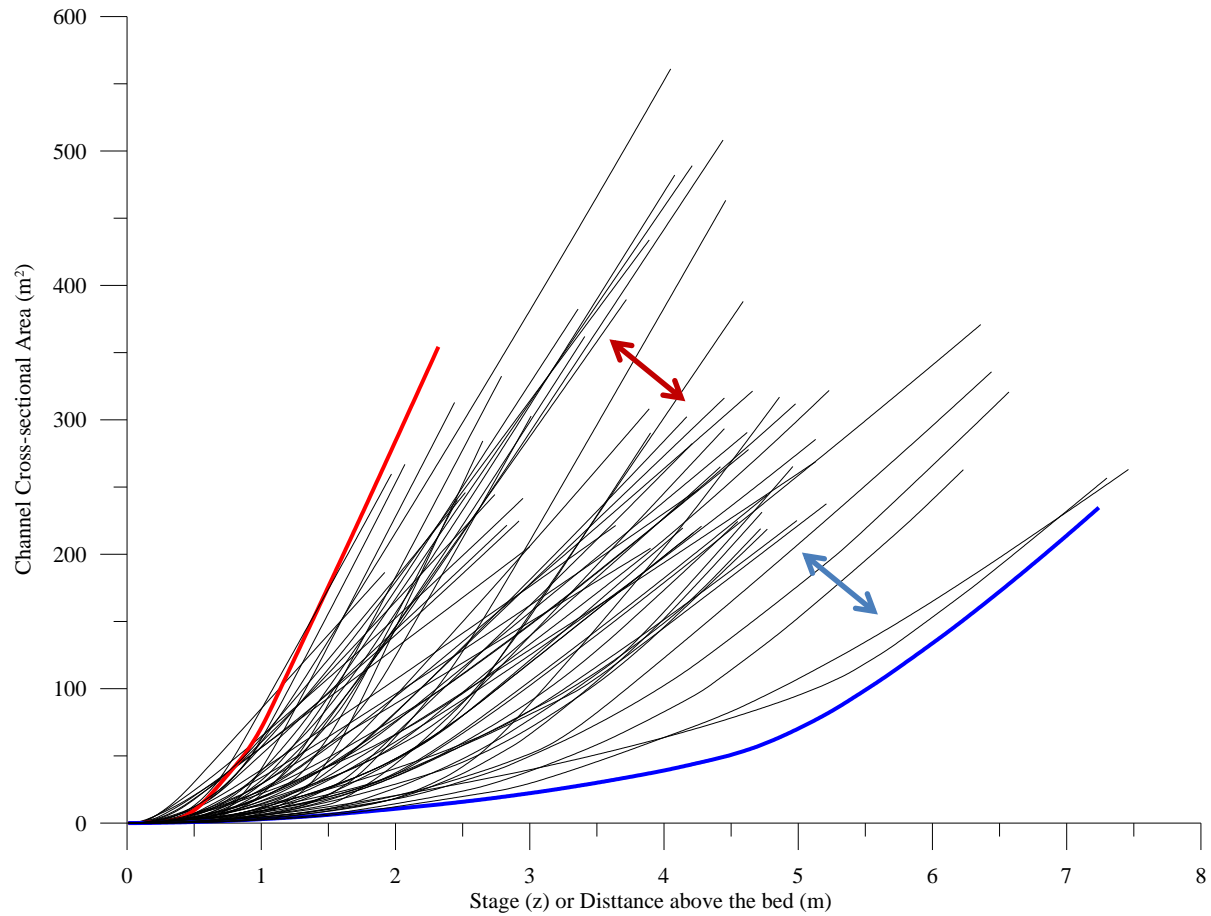
Figure 4.8 Rating curves of stage (*z*) and area (*A*). The curves represent the filling of each channel transect from the lowest channel bottom to top. The red curve represents a smaller uniform channel shape and the blue curve a larger irregular configuration. The double arrows indicate the separations among uniform, trapezoidal and irregular configurations.

increases quickly over a short stage interval. The transition from low to high slope with increasing stage is endemic to natural rivers with large undulations on the bed. When these are overtopped, *A* increases at a more uniform rate because the channel becomes wider and more uniform. This transition, or break in slope, occurs at different stages for the range of channels observed in this study. For example, the red curve of Figure 4.8 reflects a uniform shape where the break in slope occurs at a very low stage. For the blue line, however, the cross section area increases with stage at a much lower rate. The break in slope occurs at a much higher stage, and at the break in slope the rate increases, but it is much lower than the red line (Figure 4.8). The red and blue double arrows identify the range of the three categories of channel described above where the channel shape becomes increasingly irregular from red to blue.

Rating curves can be made dimensionless or proportional by normalizing each rating curve by its maximum values. These ratios are useful because they essentially remove the size effects and facilitate comparison of channel shapes without considering the channel size. The range of shapes in dimensionless rating curves is amenable to curve fitting (Figure 4.9). Here a function was applied to each curve expressed as $\mathbf{y} = \mathbf{ax^b}$ where $\mathbf{y}$ is area ratio, $\mathbf{x}$ is stage ratio, the coefficient $\mathbf{a}$ fixed at 1.0, and $\mathbf{b}$ is the free exponent of the curve fit (Figure 4.9). The increasing curvature from red to blue demonstrates increased deviation from a uniform shape of the channel, to one that is more variable, particularly with respect to the river bed. For instance, the red curve, representing the most uniform shape, may be expressed as $y = x^{1.15}$, whereas the blue line, exemplifying the most irregular shape and the greatest curvature, as $y = x^{3.07}$.

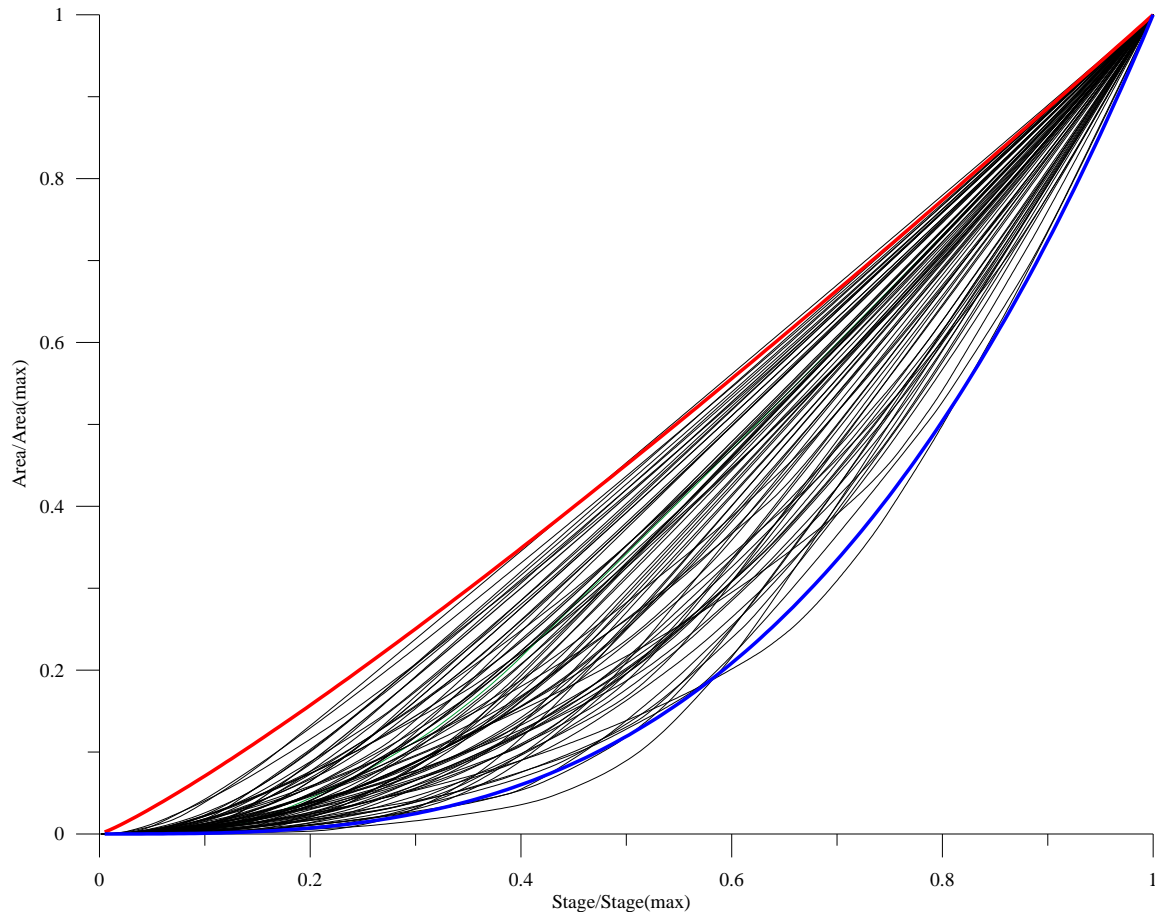All 65 channel cross sections give exponents ranging from 1.16 to 3.06 (all $R^2 >$

Figure 4.9 Non-dimensional curves of stage/stage(max) and area/area(max). The boundaries of the curves are drawn with the exponential fits by bold red and blue curves (1.15 and 3.07, respectively). The straighter the curve the more uniform the channel depth across becomes, and the more bowed the curve the more irregular the channel depth across.

0.985) with an average of 1.83±0.45. About 70% of the exponents range from 1.16 to 1.98, with this range varying from "uniform" to "trapezoid" channel types. The larger exponents from 2.15 to 3.06 correspond to the irregular channel shape. The three lowest values (1.16, 1.21 and 1.25) are outside the 95% confidence interval. Overall, the channels with the lower exponent values tend to be in the upstream and the higher values in the downstream.

4.2.5 Summary

Channel width increases exponentially in the downstream direction but channel depth does not vary in any systematic way. Average water depth, D, is typically less than 4.5 m. The $w{:}d$ values range from 14 to 163, with the population average $w{:}d$ being 38. Together, these variables reflect the characteristically wide and shallow nature of the lower Santee River channel, with a narrow range of R or efficiency values. Channel cross section areas of flow vary by a factor of ~5, and channel asymmetry estimates indicate that the majority of profiles are trapezoidal and symmetrical. Channel shapes that have been reduced to single dimensionless fit exponents demonstrate that the more uniform channels are in the upstream reach and the more irregular shapes are in the downstream.

4.3 Along-channel Variations

4.3.1 Spatial variations in cross-section asymmetry (a)

The downstream trend of a is highly irregular with relatively large values occurring primarily in the downstream and smaller values throughout (Figure 4.10).
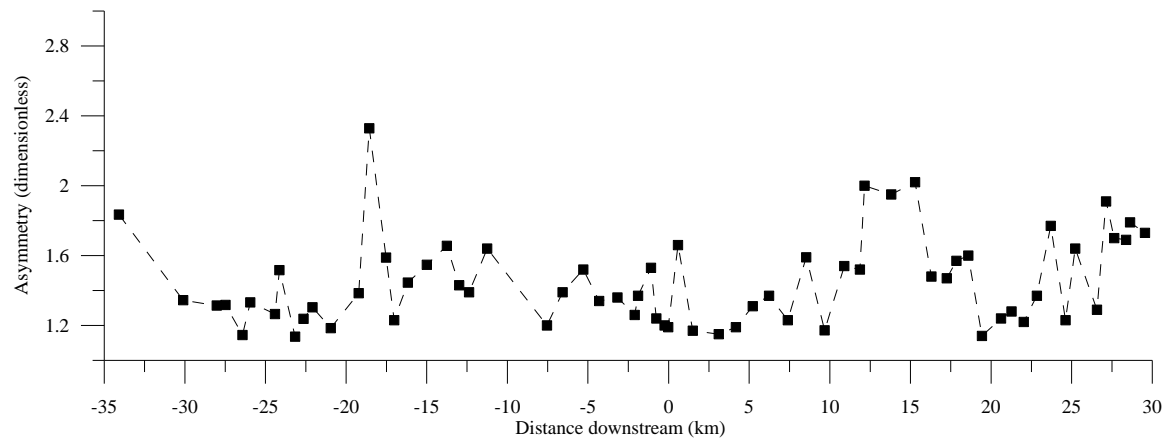
Figure 4.10 Asymmetry (*a*) variation with distance (*x*). Note the higher values and wider fluctuation that occurs in the downstream relative to upstream from +10km.

Typically the majority of the values >1.8 (75%) occur in the downstream from +13 km to +16 km and downstream from +24 km. In the upstream section from −35 km to −13 km, the values are <1.64 with only two peak values >1.8 found at −35 km and −18 km.

Separation of the upstream and the downstream is evident in the mean value of asymmetry in the upstream zone from −35 km to −10 km is 1.39±0.22. Excluding the maximum value at −18.5 km, however, the average becomes 1.36±0.17. In contrast, in the downstream section from +10 km to +30 km, the mean is 1.57±0.27. The downstream average value is higher with wider variation, and has a standard deviation that reflects the wider range of cross sections.

4.3.2 Spatial variations of width:depth ratios (w:d)

The *w:d* values are highly variable but reveal a weak trend with position along the channel. The maximum values are in the downstream reach in a range from +3 km to +22 km but with lower values interspersed (Figure 4.11). These higher values are as much as 5 times greater than those at either end of the survey reach. Also, intermediate values approaching a factor of 2 occur near the upstream limit. Hence, the overall trend from upstream to downstream begins with intermediate values that decline to minimum values from −22 km to −15 km, with the values remaining relatively low until +3 km. Subsequently, the *w:d* values fluctuate range from 10 to 160 before declining to the background values at +22 km, where they remain lower to the end of the survey. In particular, in the upstream 10<*w:d*<75, whereas in the downstream from +3 km to +30 km, wide fluctuations of 10 to 165 occur. Also, high *w:d* values are noted from +3 km to +7 km, in the same location as the bedrock outcrops. Although not statistically
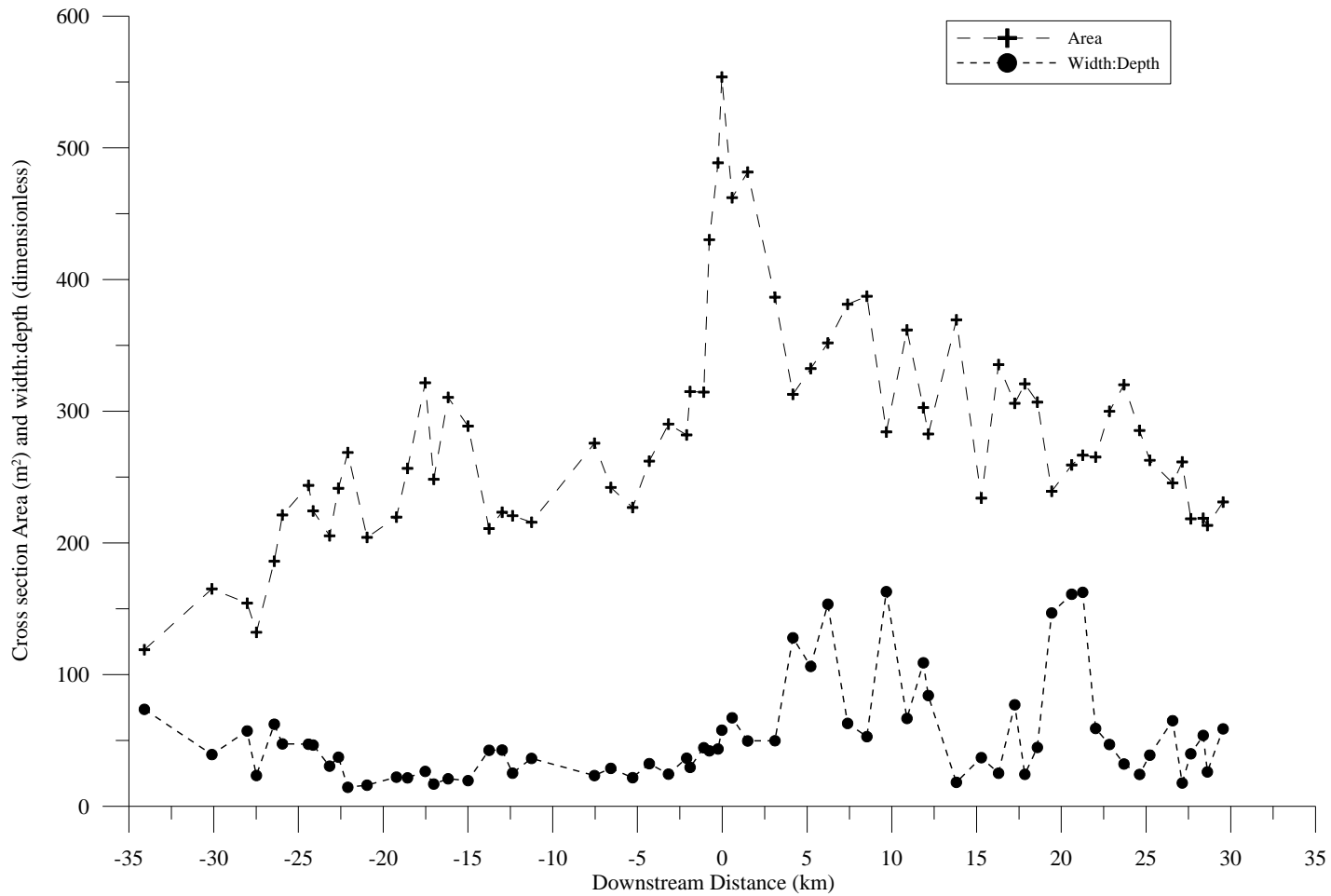
Figure 4.11 Downstream trend of width:depth ratio (*w:d*) and cross section area (*A*). Area increases with *x* in the upstream from -35 km to 0 km and decreases subsequently. The *w:*d values in relation to *x* remain relatively uniform in the upstream down to 0 km and widely fluctuate in the downstream.

significant, the *w:d* mean values upstream from +3 km and downstream from +3 km are notably different. The upstream mean value is 36.3±15 and the downstream 71.2± 47.4. The highly variable *w:d* values in the downstream likely have a strong influence on currents and perhaps also on the free surface elevation.

4.3.3 Water surface elevation and cross section area (z versus A)

The measured water surface elevations, *z*, for the range of discharges between survey days revealed slightly varying but relatively uniform slopes each day. In order to evaluate channel properties for a single discharge, the water surface elevations were matched to the lowest flow conditions, and the sloping water surface was reconstructed over the entire survey reach. The resulting water surface had a uniform decline with a slope of -6.61×10^{-2} (R^2=0.99). Considering water surface elevation as a proxy for channel distance, we plotted channel cross section area *A* versus water surface elevation *z*, or *A* vs. *z*. This association gives rise to an unexpected result in that, although *A* increases in the downstream direction at first (peaking at *z* = +2.5 m), the trend reverses further downstream (Figure 4.12). Also, a set of five particularly higher *A* values occurs at the ~2.5 m elevation, but these values are outside the 95% confidence limits.

Linear trends applied to *z* and *A* yield the pattern observed above. In the upstream where z declines from 5.5 m to 2.5 m, the linear fit is $-7.84 \mathrm{x}^{-3}$ (R^2=0.46). The extreme five *A* values at a water surface elevation of ~2.5 m form $-1.85 \mathrm{x}^{-4}$ (R^2=0.02) and correspond with ~0 km. In the downstream both *z* and *A* decrease at $8.12 \mathrm{x}^{-3}$(R^2=0.59), which is the opposite of the previous trend. These observations have led to the inference
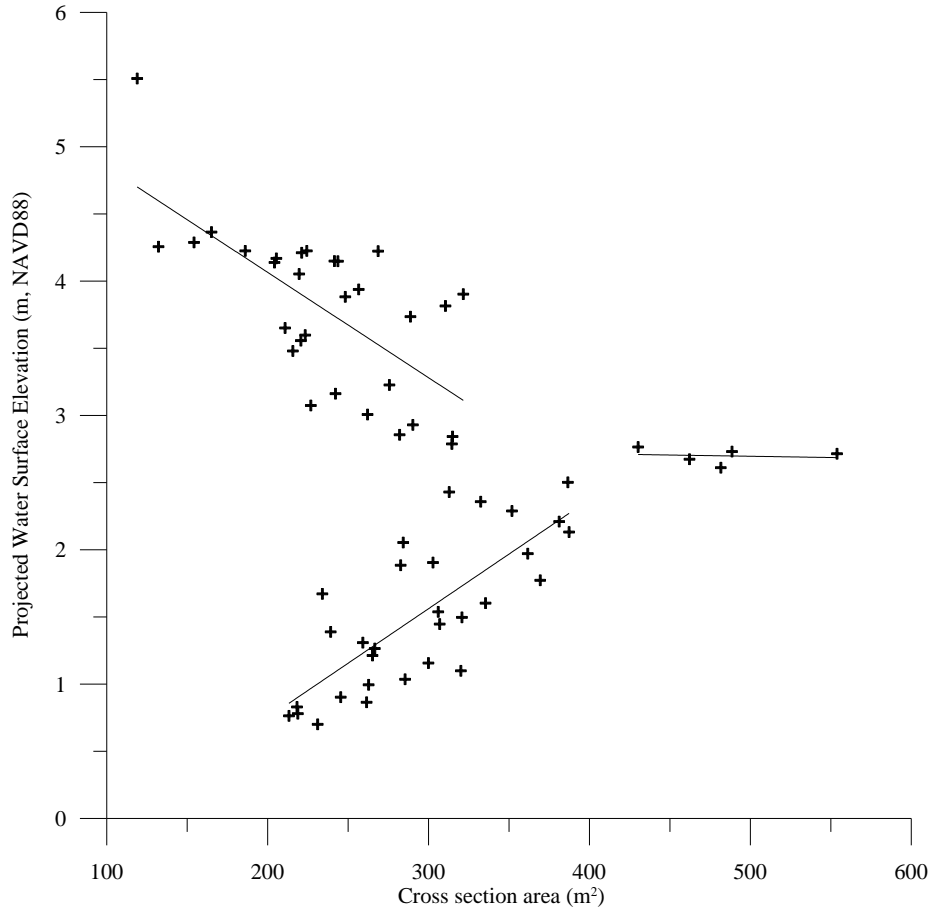
Figure 4.12 Water surface elevation (*z*) and cross section area (*A*). Cross section area has two major trends and a minor one with the continual decrease of water surface elevation. The slopes of the trend lines from high to low elevation are $-\mathbf{7.84x10^{-3}}$ (R^2=0.46), $-\mathbf{1.85x10^{-4}}$ (R^2=0.02) and $\mathbf{8.12x10^{-3}}$ (R^2=0.59). The first major trend is the increase of area with decrease of water surface elevation. A peak of abrupt increase/decrease of area occurs around 2.6 m elevation. This is followed by a decrease of area with corresponding decrease of water surface elevation.

that, during times of bankfull discharge, the water surface elevations >2.5 m correspond to the "upstream," whereas elevations <2.5 m are limited to the downstream reach.

4.3.4 Spatial variations in cross section area (x versus A)

The above observations relating z and A above translate directly to variations in A with channel location. Overall, cross section area A forms a downstream increasing trend up to the bedrock channel reach, but further downstream A tends to decrease to the end of the survey. The opposing trends in A are separated by an abrupt and large increase that begins at ~0 km (Figure 4.12). A increases from −35 km to −1 km, ranging from the minimum of 118 m^2 to 310 m^2. Over the following ~2 km, the value abruptly increases from 300 m^2 to maximum 550 m^2. Further downstream, A is highly variable but with a decreasing trend to ~200 m^2. The downstream values here are of a comparable range to those from −25 km to −10 km. Fluctuations of <140 m^2 occur in both the upstream and the downstream, most notably from −24 km to −13 km and from +8 km to +20 km.

The peak in A is a transition between the upstream and downstream trends. The values forming the abrupt increase from −5 km to 0 km are outside the 95% confidence interval, and their occurrence in the middle of the study reach is noteworthy. Interestingly, this abruptly increasing section is ~2 km upstream from where the bank bedrock outcrop occurs (from +2 km − +7 km). The bedrock zone displays an overall decrease in A, with the local low of ~300 m^2 occurring at +5 km.

The mean for the whole reach is 282 m^2±82 m^2. From −35 km to −5 km, the trend line slope is positive (3.9×10^0) or a 39-m^2 increase per km (R^2=0.49), with the mean 225 m^2±50 m^2. Excluding the abrupt increase, the trend from +3 km to +30 km is

-4.9×10^0 (R^2=0.59) or a 49-m^2 decline per km distance. The mean of 352 m^2±66 m^2 in this zone is higher than in the upstream zone.

4.3.5 Spatial variations of cross section shapes (x versus b)

The downstream trend in the dimensionless shape exponent *b* shows a net increase of up to ~10 km from ~1.3 to 2.0 (Figure 4.13). From that location the values fluctuate around an average value of 2.0. This trend indicates that the channel shape is adjusted in a systematic fashion in the downstream direction. In this case the lower upstream values indicate that the upstream channels have a more uniform and smooth shape, becoming increasingly irregular downstream. Beyond +10 km, the channel shape fluctuates strongly but consistently around a mean. This is likely in response to the effect of meanders where profiles were taken at the apex of a bend and at the straighter reaches of the meander limbs.

Upon closer inspection, one might interpret the trend as having three consecutively increasing plateaus, or three major "steps" of increase, that distinguish the upstream, midstream and downstream at −35 km to −16 km, −15 km to +6 km, and +7 km to +30 km, respectively. Each plateau is characterized by different means and ranges of values. In the upstream the value is typically <1.7 (excepting 2.4). In the midstream the range is wider (between 0.3 and 2.2), and in the downstream the range is the largest (between 1.3 and 3.0). The peak values of >2.4 are found primarily from +10 km to +30 km, excluding the one value 2.4 at −19 km. The increase in *b* with distance downstream indicates that the downstream channels tend to be more irregular. A linear correlation of *b* and *a* have a weak positive correlation of 2.99×10^{-1} (R^2=0.27).
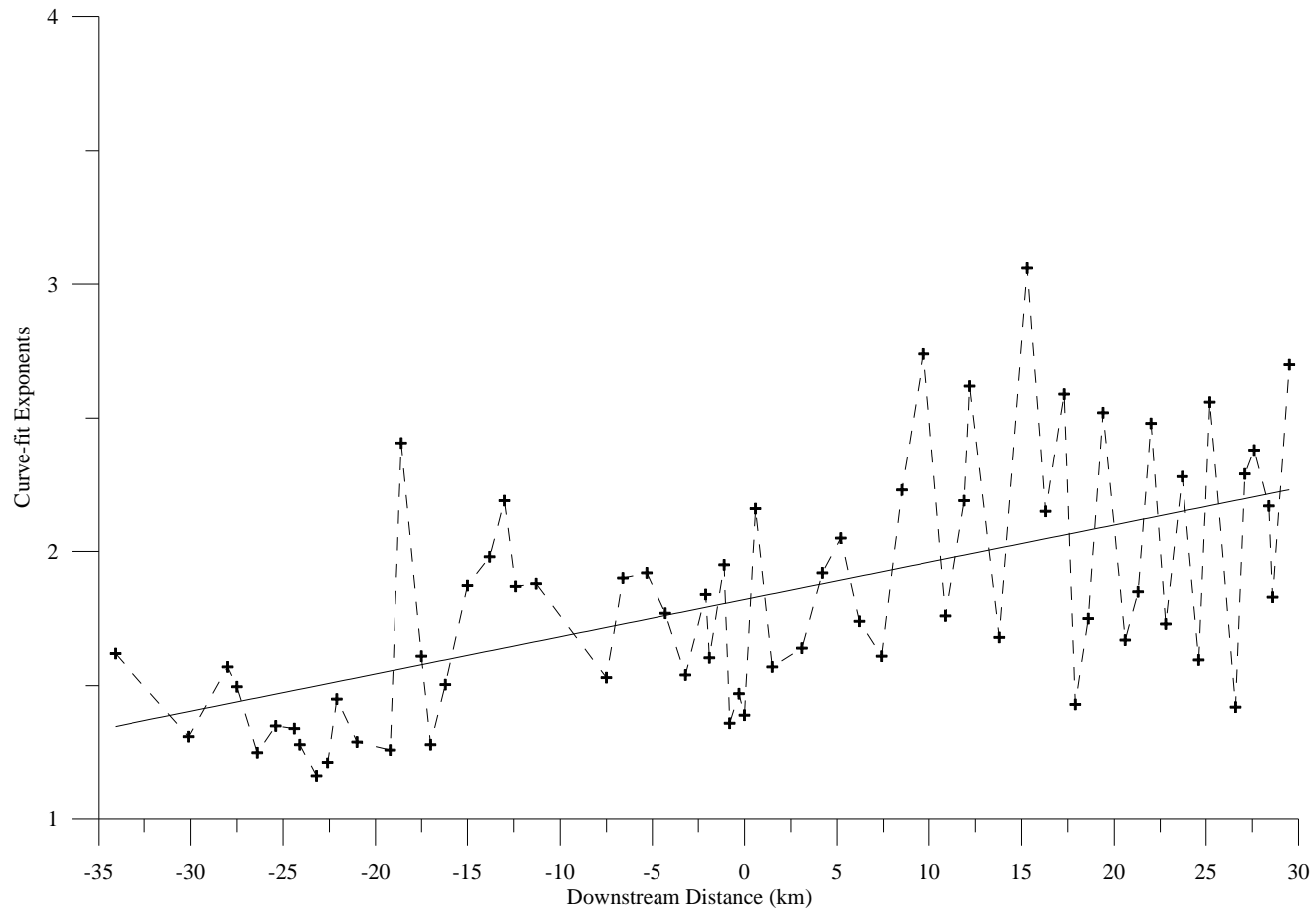
Figure 4.13 Curve-fit exponents (*b*) versus distance (*x*). The slope is 1.38×10^{-2} ($R^2=0.33$) and the value range is from 1.16 to 3.06 with a mean 1.82±0.33.

4.3.6 Summary

The assessment of channel properties z, w, $w{:}d$, A, b and a with respect to x demonstrates their overall distinction between the upstream and the downstream, and possibly their response to the bedrock. The value z decreases in the downstream throughout the reach. In the upstream section, w and $w{:}d$ remain relatively uniform. A, b and a, however, increase with x. Unexpectedly, within a short distance midstream ($<$2 km), w, $w{:}d$ and A increase abruptly. Although b and a values do not increase abruptly in relation to x, they are larger relative to their upstream values. Subsequently, with consistently low c, bedrock outcrop occurs for the next 5 km. Notably, the pattern of fluctuation begins where w and $w{:}d$ increase and A decreases. The values of w, $w{:}d$ and A decrease with x, whereas b and a continue to increase. Thus, w, $w{:}d$ and A are uniform in the upstream relative to downstream, and b and a increase with x throughout the reach.

CHAPTER 5

DISCUSSION

The flow processes and channel forms in terrestrial rivers (e.g., Leopold and Maddock 1953) and estuaries (e.g., Pillsbury 1956) have been extensively studied. However, the channel properties in reaches where the flow regime transitions from unidirectional to bidirectional have been little researched. Therefore, the main purpose of this study has been to investigate channel form in reaches where fluvial and tidal flows meet. The driving question has been: "Are there geomorphic features that characterize the fluvial-tidal transition." The Santee River channel analyses indicate that the river's geomorphic fluvial-tidal transition is inadequately explained by hydraulic geometry and tidal hydraulics.

5.1 Width and depth relationship in coastal rivers

The Santee River is located at a concave downstream end of the River Continuum. This may explain the wide w range of ~70 m to 250 m and the narrower range of D or R ~1 m to 5 m. The consequent relationship of w and R is a negative trend -8.68×10^{-3} ($R^2 = 0.33$). However, such a negative relationship between these two metrics in coastal rivers appears in the literature but has not been articulated. In terrestrial rivers, trends of w versus D are positive (e.g., Schumm 1960). Finnegan et al. (2005) also report slopes of

trend lines in *w* versus *D* that range from 5 to 59 for bedrock, boulder, cobble and gravel alpine channels. In coastal rivers, however, the relationship of *w* versus *D* is generally negative. In particular, the relationship of the two metrics at the Lower Mississippi River (Inokuchi, 1989) displays an overall trend of -8.00×10^{-3}, where a smaller *w* (~750 m) is associated with a larger *D* (~20 m) and a larger *w* (~2,000 m) with a smaller *D* (~10 m). Likewise, at the lowermost 15 km of the Incomati estuary, a smaller *D* is associated with a larger *w* and a larger *D* with a smaller *w* (Savenije 2005).

Such contrasting *w* versus *D* relationships between coastal and terrestrial rivers can be qualitatively generalized where the *w* range is larger and the *D* range is smaller in coastal rivers, and the reverse is true for terrestrial rivers (Figure 5.1). This difference is intuitive because river channel systems widen in the downstream direction and reach their maximum widths at the mouths. This factor gives rise to a negative relationship of *w* versus *D* for coastal channels and a positive relationship for terrestrial channels. We contend that these dissimilar *w* versus *D* trends are attributable to the gentle channel slope ($\sim 10^{-5}$) as a river approaches the mouth. This unexpected finding in the Santee River as well as two coastal rivers mentioned above seems to be applicable to coastal rivers worldwide.

5.2 Downstream trends

5.2.1 Sinousity (S), asymmetry (a) and cross section shape exponents (b)

A generic trend of the Santee River is represented by *S*, *a* and *b*. High *S* relates to high *a* and *b* as all channels have thalweg at the cut-bank side, with shoals toward the inner bank. The sinuous reaches from –35 km to –5 km and from +5 km to +35 km are
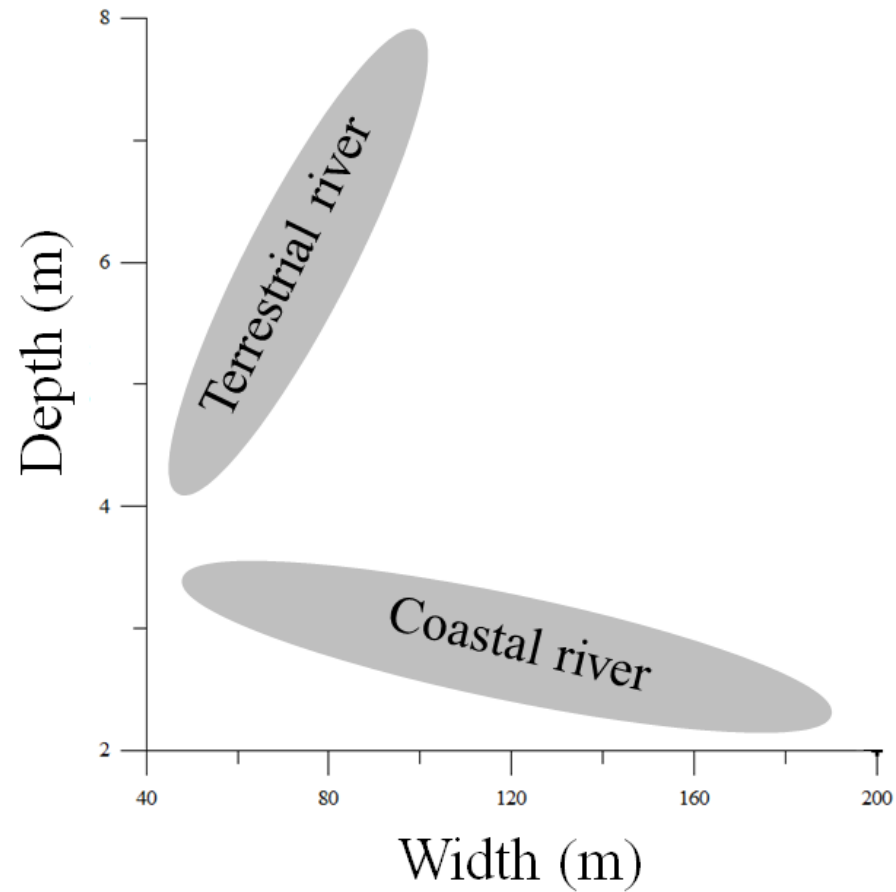
Figure 5.1 Width (*w*) and depth (*D*) relationship for terrestrial and coastal rivers. For terrestrial river channels, as width increases the depth increases, consistent with hydraulic geometry. For coastal river channels with increasing width, depth decreases. The oval for terrestrial channels modified after Schumm (1960) and Finnegan et al. (2005).

characterized as well by high *a* and high *b* (Figures 4.3, 4.10 and 4.13). Interestingly, in the Santee River the overall trends of these metrics have higher variance and larger values that occur in the downstream. For instance, for *S* the widest range of values are accompanied by five out of seven peak values from +13 km to +35 km. For *a* the majority of the peak values >1.6 occur from +10 km to +30 km. For *b* the values that are >2.1 as also the peak value (3.06) are found from +9 km to +30 km. These trends are a simple indication that the downstream zone is featured by highly sinuous, asymmetrically irregular shapes.

5.2.2 Riverbed

The Santee riverbed crosses all three tidal elevations projected from the coast. Presumably, from the upstream to the downstream the flow regime in the channel is driven increasingly less by topography and more by tides. As such, channel morphology in the downstream zone from +5 km to +30 km appears less fluvial than the upstream half from −35km to −5km. For instance, the upstream reach is marked by progressive

uniform decreases in bed and thalweg elevation before starting to fluctuate in the downstream from ~0 km. Such a higher gradient is necessary because unidirectional flows are driven solely by the topographic gradient. However, since the middle and lower part of the upstream section crosses the tidal elevations and the gaging data show current reversals at low discharges, we suggest that the upstream from −35 km to −5 km is fluvial-dominant with less tidal influence on the channel.

Downstream of the slope break and bedrock (+7 km to +30 km) are marked bed elevation fluctuations and "deeps." These trends are reflected in larger running standard

deviation values of the riverbed. Interestingly, such increased fluctuations of the riverbed downstream from such a slope break have been reported elsewhere. For instance, the long profile analysis in the Lower Mississippi River shows wider fluctuations of the bed and more "deeps" in the downstream reaches (Harmar and Clifford 2007). Additionally, in the downstream zone—from ~500 km upstream to the "mouth" (Head of Passes)—the approximate bed gradient is lower and the variance larger relative to the upstream section (from ~900 km to ~500 km, measured from the "mouth"). The authors attributed the deeps solely to low bank erodibility, but we suspect that such bed fluctuations in the downstream are partially related to fluvial-tidal processes. Although current reversals are rare in the Lower Mississippi River—for example, near Belle Chasse, LA (~ 130 km upstream from the "mouth"; see Demas 2012)—backwater effects occur as far upstream as 800 km from the "mouth" (Inokuchi 1989).

5.2.3 Cross sections

The general trends of *w* and *w:d* in the Santee River remain relatively uniform overall but *A* increases in the downstream direction from −35 km to −2 km. The relatively gradual increase of *A* is consistent with downstream hydraulic geometry (e.g., Leopold and Maddock 1953). However, from −2 km to 0 km these values increase abruptly. The increases are peculiar because they coincide with the riverbed slope break. We suggest that the abrupt increase of the dimensions constitutes a fluvial-tidal transition. We concur with Yankovsky et al. (2012) that the feedback relationship of tidal energy dissipation and the upstream direction convergence occurs in a relatively short distance.

Subsequently, from +2 km to +30 km, w, $w:d$ and A decrease overall with fluctuations. Notably, decreased dimension values occur from +25 km to +35 km that are close to the upstream values from −25 km to −5 km. The dimensional trend of the abrupt increase and decrease of A is contrary to fluvial hydraulic geometry (e.g., Leopold and Maddock 1953) and tidal hydraulics (e.g., Pillsbury 1956; Savenije 2005). These two principles describe the increase of w, d and A in the downstream direction in terrestrial and tidal channels toward the mouth. The discrepancy between our data and hydraulic geometry suggests that this channel section of the Santee River (from ~+2 km to +30 km) is neither fully fluvial nor fully tidal but rather fluvial-tidal—a geomorphic fluvial-tidal transition. That the four highest values of abruptly increased A is outside the 95% confidence interval bolsters our view. We therefore hypothesize that backwater effects on the unidirectional flow by flood tide give rise to these anomalous channel properties.

5.2.4 Backwater effects and the geomorphic fluvial-tidal transition model

Backwater effects occur when any unidirectional channel flow is obstructed. For instance, logjams and beaver dams inhibit river flows and lead to a water depth increase, aggradation and overbank flows in the immediate upstream (e.g., Wohl and Beckman 2014). Upstream from the impoundment, the water volume will be larger than where there is no hindrance to the flow. Likewise, at a fluvial-tidal transition, the flood tide acts as a semi-diurnal blockage that is mobile along the channel. Flood tides obstruct the river discharge, which leads to larger water retention in the upstream like a reservoir behind a dam. Over time, with the continuous semi-diurnal filling of the reach, the channel would have to enlarge in order to accommodate the larger water volume. The application of

backwater effects to fluvial-tidal channel suggests that the abrupt increases followed by the decreases of *w*, *w:d* and *A* over ~30 km downstream are a shape sculpted by backwater effects.

Applying backwater effects on the peculiar Santee River properties, we have developed a conceptual model for fluvial-tidal transition (Figure 5.2). River continuum in the coastal plain contains terrestrial and tidal parts. Migrating downstream, the channel transitions from Terrestrial to Tidal, with *w* or *A* increasing overall. The fluvial-tidal transition consists of Head of tide, Backwater effect limit, Salinity transition and Sedimentary transition. The channel form changes drastically within the Geomorphic transition, which encompasses the zones of Backwater effect limit and the immediate upstream section of Salinity transition. From Fluvial response to tide to the Fluvial-Tidal Bridge, the terrestrial river transitions to the tidal estuary. Our study site spans between the Salinity transition and possibly upstream of the Head of tide. In the Geomorphic transition, flood tide causes backwater effects that increase water volume in the upstream. Downstream from the decrease of *w* and *A* in the Fluvial-Tidal Bridge is bidirectional flow, which is more dominant than flow blockage. Recurrence of the tidal process over a prolong period of time would augment the channel between the Backwater effect limit and the Salinity transition, thus creating the Geomorphic transition.

5.3 Potential complications due to bedrock

The coincidence of the Geomorphic fluvial-tidal transition with bedrock (from +2 km to +7 km) could be considered a weakness of the interpretation that backwater effects are

responsible for the peculiarities in the Santee River. Three major reasons why the bedrock influence is insignificant include the width trends in a terrestrial river that contains alluvial-bedrock reaches, the feedback relationship of tidal energy and channel morphology, and observations in other rivers that are similar to the Santee River. These reasons will be discussed below.

5.3.1 Widening at an alluvial-bedrock channel

The Santee River w increases by 70% at the alluvial-bedrock transition. However, width variations of the alluvial-bedrock reaches of a non-tidal river illustrate a negligible effect of bedrock on w; Keen-Zebert and Curan (2009) report the w of the Upper Guadalupe River at its bedrock sections (28 m±8.9 m) that are merely 7% wider than its alluvial reaches (26 m±9.0 m). Such a meager difference of w in a non-tidal river and the large difference of w in the tidal Santee River at its alluvial-bedrock reach suggest that the bedrock influence in the Santee River is negligible. Hence, the bedrock presence in the Santee may not necessarily be a main contributor of the abruptly widening channel.

5.3.2 Morphology and tide energy

Yankovsky et al. (2012) concluded that fluvial-tidal processes and the channel form interact in the reach of strong convergence, or abrupt increase in w and A in the downstream. Here, a feedback loop exists as tidal energy is rapidly dissipated due to the upstream convergence in the transition zone, and the process of energy dissipation modifies the channel morphology. The authors' conclusion was based on estimations of tidal energy dissipation and channel morphology, and was not hindered by the bedrock in
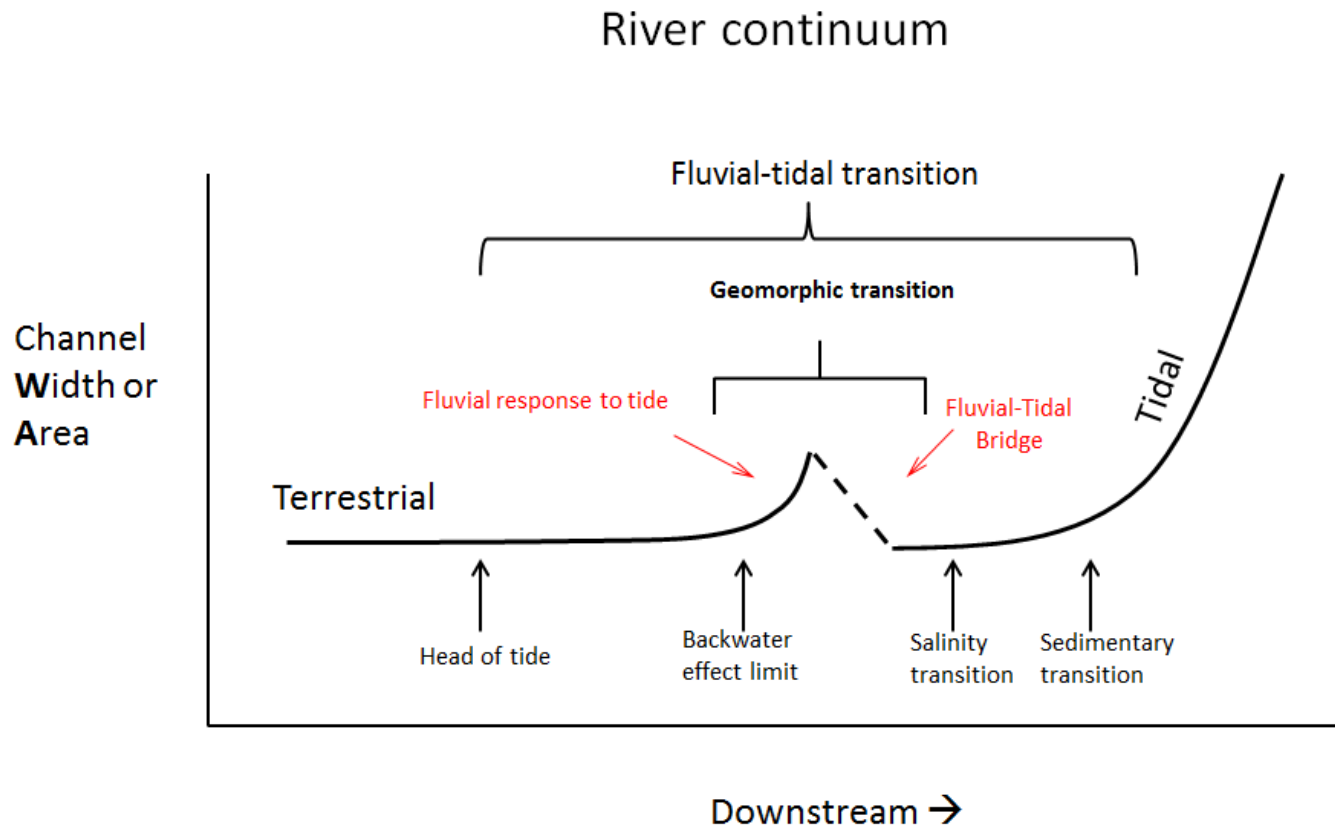
Figure 5.2 Conceptual model of fluvial-tidal transition. The river continuum with the conceptual fluvial-tidal transition highlighted. From upstream to downstream, there exist the Head of tide, Backwater effect limit, Salinity transition and Sedimentary transition. Between the Backwater effect limit and Salinity transition, there is the Geomorphic transition of the channel that contains the Fluvial response to tide and the Fluvial-Tidal bridge. These show a marked increase and decrease in width and area over a relatively short distance.

the vicinity (for similar interactions between channel shape and tidal wave, see also Wright et al. 1973; Lanzoni and Seminara 1998).

5.3.3 Similar observations in other rivers

The Fluvial Response to tide and Fluvial-Tidal Bridge may be prevalent in other coastal plain rivers reported in the literature, which reinforces our indifference of the bedrock presence in the Santee River. The following works unwittingly have overlooked the anomalous channel trends as shown in the Santee River. Inokuchi (1989) presented the plots of the cross section w, d, and A of the Lower Mississippi River. At ~200 km–400 km inland from the mouth, A and w appear to be decreasing in the downstream direction. For example, in this section A increases abruptly from 1,400 m^2 to 1,700 m^2 for 50 km downstream and decreases gradually to 1,500 m^2 for 250 km. Friedrichs (2006) showed river valley estuaries—Potomac, Delaware, James and Rappahannock—all of which have pronounced decrease of A in 10s of km in the downstream direction. Ensign et al. (2012, 2014) likewise present narrowing of channels in the downstream direction. Such previously unnoticed trends of w and/or A versus distance data from other coastal rivers strengthen the case for a geomorphic fluvial-tidal transition.

5.4 Summary

The negative w versus D or R relationships, the increasing fluctuations of the riverbed elevation and thalweg in the downstream reaches, and the abrupt increase and following decrease of w, $w{:}d$ and A in the downstream—all of these are some peculiarities of the freshwater tidal Santee River. Especially the w and A trends are in

contrast to hydraulic geometry and tidal hydraulics. We conclude that these features are intrinsic to coastal plain rivers and are the signatures of backwater effects induced by tides in the fluvial-tidal transition. We therefore expect that these are likely to be found worldwide.

CHAPTER 6

CONCLUSIONS

In geomorphology, process and form are interrelated, where flow processes and channel form influence one another in a feedback relationship (e.g., Richards 1982). Presumably, in freshwater channel reaches where both riverine and estuarine flows coexist, a channel would form that is distinct from fully fluvial channels or fully tidal counterparts. Analyses of the Santee River suggest that there are intrinsic channel properties at the fluvial-tidal flow juncture, namely, a geomorphic fluvial-tidal transition. In the upstream zone, the channel resembles a terrestrial river that features relatively uniform trends in cross section area (A), width (w) and depth (D) in the downstream direction (~30 km) and overall descending riverbed elevations. In the downstream zone, however, A, w and D sharply increase and then markedly decrease over a short distance (~30 km). In this short reach, the riverbed also fluctuates irregularly while maintaining an overall low-gradient (10^{-5}). These trends of abrupt increase and marked decrease in the channel dimensions downstream, as also the increasing fluctuations of the riverbed, are distinct features of fluvial-tidal channel transition, sculpted primarily by backwater effects. The Santee River's fluvial-tidal transition channel form is distinct from fully terrestrial and fully estuarine channels. Similar results should be found in other coastal plain rivers, as other reports in the literature seem to corroborate our findings.

<center>REFERENCES</center>

Allen, George P. 1991. Sedimentary processes and facies in the Gironde Estuary: A recent model for macrotidal estuarine systems, in *Clastic Tidal Sedimentology*, edited by DG Smith, E Reinson, BA Zaitlin, RA Rahmani, *Canadian Society for Petroleum Geologists*, Memoir 16, 29-40.

Ashley, Gail M., William H. Renwick. 1983. Channel morphology and processes at the riverine-estuarine transition, the Raritan River, New Jersey, *Special Publications of International Association of Sedimentologists,* 6, 207-218.

Ashley, Gail M., William H. Renwick, Gary H. Haag. 1988. Channel form and process in bedrock and alluvial reaches of the Raritan River, New Jersey, *Geology*, 16, 436-439.

Bird, Eric. 2008. Coastal Geomorphology: An Introduction (2nd ed). Wiley, West Sussex, England.

Blum, Michael D., Torbjörn E. Tornqvist. 2000. Fluvial responses to climate and sea level change: A review and look forward, *Sedimentology*, 47, 2-48.

Bukaveckas, Paul A, L.E. Barry, MJ Beckwith, V David, B Lederer. 2011. Factors determining the location of the chlorophyll maximum and the fate of algal production with the tidal freshwater James River, *Estuaries and Coasts*, 34, 569-582.

Bokuniewicz, Henry. 1995. Sedimentary systems of coastal plain estuaries, in: GME Perillo, ed., *Geomorphology and Sedimentology of Estuaries*, 49-67, Elesevier Science, Amsterdam.

Campbell, Bruce G, Alissa L Coes. (Eds.) 2011. Groundwater Availability in the Atlantic Coastal Plain of North and South Carolina, *USGS Professional Paper 1773,* Groundwater Resources Program.

Cattaneo, Antonio, Ron J. Steel. 2003. Transgressive deposits: a review of their variability, *Earth Science Reviews*, 62, 187-228.

Colquhoun, David J. 1968. Coastal Plains, in: RW Fairbridge, ed., *The Encyclopedia of Geomorphology*, Reinhold Book Corp., 144-150.

Cornwell, Kevin, Doug Norsby, Richard Marston. 2003. Drainage, sediment transport, and denudation rates on the Nanga Parbat Himalaya, Pakistan, *Geomorphology*, 55, 25-43.

<center>58</center>

Dalrymple, Robert W., Brian A. Zaitlin, Ron Boyd. 1992. Estuarine facies models: conceptual basis and stratigraphic implications. *Journal of Sedimentary Petrology*, 62(6) 1130-1146.

Dalrymple, Robert W. and Kyungsik Choi. 2007. Morphologic and facies trends through the fluvial-marine transition in tide-dominated depositional systems: A schematic framework for environmental and sequence-stratigraphic interpretation, *Earth-Science Review*. 81, 135-174.

Dalrymple, Robert W., Duncan A. Mackay, Aitor A. Ichaso, Kyungsik S. Choi. 2012. Processes, morphodynamics, and facies of tide-dominated estuaries, in RA Davis and RW Dalrymple, Eds., *In Principles of Tidal Sedimentology*, Springer Science, 79-107.

Demas, Alex. 2012. Mississippi River Flows Backwards Due to Isaac, United State Geological Survey Newsroom, Aug 29, 2012. Accessed May 30, 2014.

Eckard TL. 1983. Stratigraphy and Depositional History of the Santee River Delta, South Carolina, University of South Carolina, Columbia, S.C.

Ensign, Scott H., Martin W. Doyle, Michael F. Piehler. 2012. Tidal geomorphology affects phytoplankton at the transition from forested streams to tidal rivers. *Freshwater Biology* 57, 2141-2155.

Ensign, Scott H., Martin W. Doyle, MF Piehler. 2013. The effect of tide on the hydrology and morphology of a freshwater river. *Earth Surface Processes and Landforms*. 38, 655-660.

Ensign, Scott H., Gregory B. Noe, Cliff R. Hupp. 2014. Linking channel hydrology with riparian wetland accretion in tidal rivers. *Journal of Geophysical Research-Earth Surface*. 119(1), 28-44.

Finnegan, Noah J., Gerard Roe, David R. Montgomery, Bernard Hallet. 2005. Controls on the channel width of rivers: Implications for modeling fluvial incision of bedrock. *Geology* 33(3), 229-232.

Florsheim, Joan L., Jeffrey F. Mount, Christopher Hammersmark, William E. Fleenor, Geoffrey S. Schladow. 2008. Geomorphic Influence on Flood Hazards ina Lowland Fluvial-Tidal Transitional Area, Central Valley, California. Natural Hazard Review 9(3), 116-124.

Friedrichs, Carl T. 2006. Tides in equilibrium river valley estuaries. *Physics of Estuaries and Coastal Seas*.

Godin, G. 1999. The propagation of tides up rivers with special considerations on the upper Saint Lawrence River, *Estuarine, Coastal, and Shelf Science*, 48, 307-324.

Gurnell, Angela M. 1997. Adjustments in river channel geometry associated with hydraulic discontinuities across the fluvial tidal transition, *Earth Surface Processes and Landforms*, 22, 967-985.

Hardy, Thomas, Palavi Panja, and Dean Mathias. 2005. *WinXSPRO, a channel cross section analyzer, user's manual, Version 3.0*. Department of Agriculture, Forest Service, Rocky Mountain Research Station: Fort Collins.

Harmar, Oliver P., Nicholas J. Clifford. 2007. Geomorphological explanation of the long profile of the Lower Mississippi River. *Geomorphology* 84, 222-240.

Hockensmith, Brenda L. 2004. Flow and salinity characteristics of the Santee River Estuary, SC, SCDNR *Water Resources Report 35*, 96p.

Hodge, John A. 1981. Erosion of the North Santee River Delta and Development of a Flood-Tidal Complex, University of South Carolina, Columbia, S.C.

Horrevoets, AC, Hubert H.G. Savenije, JN Schuurman, S Graas, 2004. The influence of river discharge on tidal damping in alluvial estuaries. *Journal of Hydrology,* 294, 213-228.

Hughes, W. Brian. 1994. National water-quality assessment program- the Santee River Basin and coastal drainages, NC and SC. *U.S. Geological Survey*. Fact Sheet, FS-010-94

Inokuchi, Masao. 1989. Channel Morphology of the Lower Mississippi River, *Trans of the Jap. Geomorh. Union*, 19, 83-94.

Jay, David A., 1991. Green's law revisited: tidal long wave propagation in channels with strong topography. *Journal of Geophysical Research,* 96: 20,585-20.

Keen-Zebert, Amanda, Joanna C. Curran, 2009. Regional and local controls on the spatial distribution of bedrock reaches in the Guadalupe River, Texas, *Geomorphology*, 112, 295-305.

Kjerfve, Björn, J.E. Greer. 1978. Hydrography of the Santee River during moderate discharge conditions, *Estuaries*, 1, 111-119.

Knighton, David. 1984. *Fluvial Forms and Processes*. Edward Arnold (repri. 1987) Baltimore, MD.

Lanzoni, Stefano, and Giovanni Seminara. 1998. On tide propagation in convergent estuaries. *J. Geophys. Res*., 103, 30793-30812.

Lapine, Lewis A., Matthew J. Wellslager. 2007. GPS and GLONASS for precision, SC's GNSS virtual reference network, *InsideGNSS*, July, 50-57.

Langbein, Walter B. 1963. The hydraulic geometry of a shallow estuary. *Bull. Int. Assoc. Sci. Hydrol.* 8, 84-94.

Leopold Luna B., Thomas Maddock. 1953. The hydraulic geometry of stream channels and some physiographic implications. *USGS Prof. Paper 252*.

Leopold, Luna B., M. Gordon Wolman and John P. Miller. 1964. Fluvial Processes in Geomorphology. Dover Publications (republication in 1992), Mineola, NY.

Milliman, John D. and Katherine L. Farnsworth. 2005. River runoff, Erosion and
Delivery to the Coastal Ocean; a Global Analysis, Cambridge University Press.

National Oceanic and Atmospheric Administration—National Geodetic Survey, for the
tidal benchmarks, web accessed Aug 5, 2013.

Nitsche, Frank O., Robin Bell, Suzanne M. Carbotte, William B.F. Ryan, Roger Flood.
2004. Process related classification of acoustic data from the Hudson River
estuary, *Marine Geology*, 209, 131-145.

Odum, William E. 1988. Comparative ecology of tidal freshwater and salt marshes. *Ann.
Rev. Ecul. Sysl.*, 19, 147-76.

Phillips, Jonathan D., Michael C. Slattery. 2007. Downstream trends in discharge, slope,
and stream power in a lower coastal plain river, *Jour. of Hydrol*. 334, 290-303.

———. 2008. Antecedent alluvial morphology and sea level controls on from-process
transition zones in the lower Trinity River, Texas, *River Res. Appl*. 34, 293-309.

Pillsbury, George B. 1956. Tidal hydraulics (rev. ed.): *Corps of Engineers, U.S. Army.*

Renwick, William H, Gail M. Ashley. 1984. Sources, storages, and sinks of fine-grained
sediments in a fluvial-estuarine system, *Geol. Soc. of Am. Bull.*, 95, 1343-1348.

Richards, Keith. 1982. River: Form and Process in Alluvial Channels, Blackburn Press,
New Jersey.

Sandercock, Peter J. and Hooke JM. 2010. Assessment of vegetation effects on
hydraulics and of feedbacks on plant survival and zonation in ephemeral channels.
Hydrological Processes, 24, 695-713.

Savenije, Hubert H.G. 2005. Salinity and Tides in Alluvial Estuaries, Elsevier, the
Netherlands.

Savenije, Hubert H.G., Marco Toffolon, Jennifer Haas, Ed J.M. Veling. 2008. Analytical
description of tidal dynamics in convergent estuaries. *Journal of Geophysical
Research*. 113, doi:10.1029/2007JC004408.

Schumm, Stanley A. 1960. The shape of alluvial channels in relation to sediment type:
U.S. Geological SurveyProfessional Paper 352-B, 17–30.

Schumm, Stanley A and RW Lichty. 1965. Time, space and causality in geomorphology,
Am. Jour. of Sci, 263, 110-119.

Schumm, Stanley A. 1977. The Fluvial System. John Wiley & Sons, Inc.

Siple, G.E. 1960. Some geologic and hydrologic factors affecting limestone terraces of
Tertiary age in South Carolina, *Southeastern Geology*, *2*, 1-11.

Soulsby, Richard. 1997. *Dynamics of marine sands: A manual for practical application*,
249 pp., Thomas Telford Publications, London, United Kingdom.

van den Berg, Jan H., JR Boersma, A van Gelder. 2007. Diagnostic sedimentary structures at the fluvial-tidal transition zone-Evidence of the depostits from the Rhine and Meues, *Netherlands Jour. of Geosci.*, 86, 287-306.

Walker, Jason. 2011. Channel processes and form near the tidal limit, Master's Thesis, University of South Carolina.

Wohl, Ellen, Natalie D. Beckman. 2014. Leaky rivers: implications of the loss of longitudinal fluvial disconnectivity headwater streams. *Geomorphology*, 205, 27-35.

Wright LD, JM Coleman, BG Thom. 1973. Process of channel development in a high-tide range environment: Cambridge Gulf-Ord River Delta, Australia, *Jour. of Geol.*, 81, 15-41.

Yankovsky, Alexander E, Raymond Torres, Legna Torres-Garcia, Kyungho Jeon. 2012. Interaction of tidal and fluvial processes in the transition zone of the Santee River, SC, USA, *Estuaries and Coasts*, 35(6), 1500-1509.

APPENDIX A: MATLAB SCRIPTS

This appendix includes the Matlab scripts employed in the data analyses as well as some results that are unreported in the main text.

A. Matlab scripts used for analyses

The data analyses involved Matlab scripts for long profile data and for cross section data. The 5-m interpolation and the 5-km running standard deviation were acquired using the scripts given below.

A.1 The interpolation script

The long profile field survey was set at a 5-m interval to assure a consistent data interval, the riverbed elevation was interpolated using the following script.

```
A=["Raw distance" "Depth"];

% Get distance from loaded data
x1 = A(:,1);
% Get depths from loaded data
h1 = A(:,2);

a=diff(x1);

j=find(a==0);
x1(j)=[];
h1(j)=[];

% Create new x with 5 m differences
```

```matlab
x2 = min(x1):5.0:max(x1);
% Interpolate the data from original x1 and h1 for x2.
h2 = interp1(x1,h1,x2);
h3=h2';
x3=x2';

% the distance-interpolated final product.
XH=[x3,h3];
```

A.2 The 5-km running standard deviation

The script used for the running standard deviation of the riverbed (Figure 4.1B)

was designed by John D'Errico and obtained from the Mathworks Matlab forum (URL:

http://www.mathworks.com/matlabcentral/fileexchange/9428-moving-window-standard-

deviation/content/movingstd.m, accessed 5/21/2014). The script is reproduced below:

```
function s = movingstd(x,k,windowmode)
% movingstd: efficient windowed standard deviation of a time series
% usage: s = movingstd(x,k,windowmode)
%
% Movingstd uses filter to compute the standard deviation, using
% the trick of std = sqrt((sum(x.^2) - n*xbar.^2)/(n-1)).
% Beware that this formula can suffer from numerical problems for
% data which is large in magnitude.
%
% At the ends of the series, when filter would generate spurious
% results otherwise, the standard deviations are corrected by
% the use of shorter window lengths.
%
% arguments: (input)
%  x   - vector containing time series data
%
%  k   - size of the moving window to use (see windowmode)
%        All windowmodes adjust the window width near the ends of
%        the series as necessary.
%
%        k must be an integer, at least 1 for a 'central' window,
%        and at least 2 for 'forward' or 'backward'
%
%  windowmode - (OPTIONAL) flag, denotes the type of moving window used
%        DEFAULT: 'central'
%
%        windowmode = 'central' --> use a sliding window centered on
%            each point in the series. The window will have total width
%            of 2*k+1 points, thus k points on each side.
%
%        windowmode = 'backward' --> use a sliding window that uses the
%            current point and looks back over a total of k points.
%
%        windowmode = 'forward' --> use a sliding window that uses the
%            current point and looks forward over a total of k points.
%
%        Any simple contraction of the above options is valid, even
%        as short as a single character 'c', 'b', or 'f'. Case is
%        ignored.
%
% arguments: (output)
%  s   - vector containing the windowed standard deviation.
%        length(s) == length(x)
```

```matlab
% check for a windowmode
if (nargin<3) || isempty(windowmode)
  % supply the default:
  windowmode = 'central';
elseif ~ischar(windowmode)
  error 'If supplied, windowmode must be a character flag.'
end
% check for a valid shortening.
valid = {'central' 'forward' 'backward'};
windowmode = lower(windowmode);
ind = strmatch(windowmode,valid);
if isempty(ind)
  error 'Windowmode must be a character flag: ''c'', ''b'', or ''f''.'
else
  windowmode = valid{ind};
end

% length of the time series
n = length(x);

% check for valid k
if (nargin<2) || isempty(k) || (rem(k,1)~=0)
  error 'k was not provided or not an integer.'
end
switch windowmode
  case 'central'
    if k<1
      error 'k must be at least 1 for windowmode = ''central''.'
    end
    if n<(2*k+1)
      error 'k is too large for this short of a series and this
windowmode.'
    end
  otherwise
    if k<2
      error 'k must be at least 2 for windowmode = ''forward'' or
''backward''.'
    end
    if (n<k)
      error 'k is too large for this short of a series.'
    end
end

% Improve the numerical analysis by subtracting off the series mean
% this has no effect on the standard deviation.
x = x - mean(x);

% we will need the squared elements
x2 = x.^2;

% split into the three windowmode cases for simplicity
A = 1;
switch windowmode
  case 'central'
    B = ones(1,2*k+1);
```

```matlab
      s = sqrt((filter(B,A,x2) - (filter(B,A,x).^2)*(1/(2*k+1)))/(2*k));
      s(k:(n-k)) = s((2*k):end);
    case 'forward'
      B = ones(1,k);
      s = sqrt((filter(B,A,x2) - (filter(B,A,x).^2)*(1/k))/(k-1));
      s(1:(n-k+1)) = s(k:end);
    case 'backward'
      B = ones(1,k);
      s = sqrt((filter(B,A,x2) - (filter(B,A,x).^2)*(1/k))/(k-1));
end

% special case the ends as appropriate
switch windowmode
  case 'central'
    % repairs are needed at both ends
    for i = 1:k
      s(i) = std(x(1:(k+i)));
      s(n-k+i) = std(x((n-2*k+i):n));
    end
  case 'forward'
    % the last k elements must be repaired
    for i = (k-1):-1:1
      s(n-i+1) = std(x((n-i+1):n));
    end
  case 'backward'
    % the first k elements must be repaired
    for i = 1:(k-1)
      s(i) = std(x(1:i));
    end
end

% catch any complex std elements due to numerical precision issues.
% anything that came out with a non-zero imaginary part is
% indistinguishable from zero, so make it so.
s(imag(s) ~= 0) = 0;
```

67

A.3 Orthogonal projection for cross sections

The following orthogonal projection code was designed to align points across the

channel that deviated from a straight line.

```
% 1) The RELATIVE easting, northing, depth data below.
UTM=[ "Easting", "Northing", "Depth"];

% 2) set the Left bank value and the Right bank value to find the line
equation of (y2-y1)/(x2-x1). (Mapview slope)
v=[1,-0.5596];

% 3) the line equation (figure out from the relative UTM)
easting=UTM(:,1); northing=UTM(:,2);
cUTM = [easting, northing];

% 4) type in 1 through the number (#) of rows there are, i.e. (1:#).
% Start a For loop:
for i = 1:"# of points";

    pUTM(i,:)=(dot(v,cUTM(i,:))/dot(v,v))*v;
end
xyz=[pUTM, UTM(:,3)];

% 5) the straight line across the channel.
real_xyz = sortrows(xyz);
```

B. Additional results unreported in the main text

The following results were unreported in the main part of the study: a running mean riverbed with slope breaks, the relationship of sinuosity (*S*) versus asymmetry (*a*), and the trends of natural log-transformed width (*w*), depth (*D*) and area (*A*).
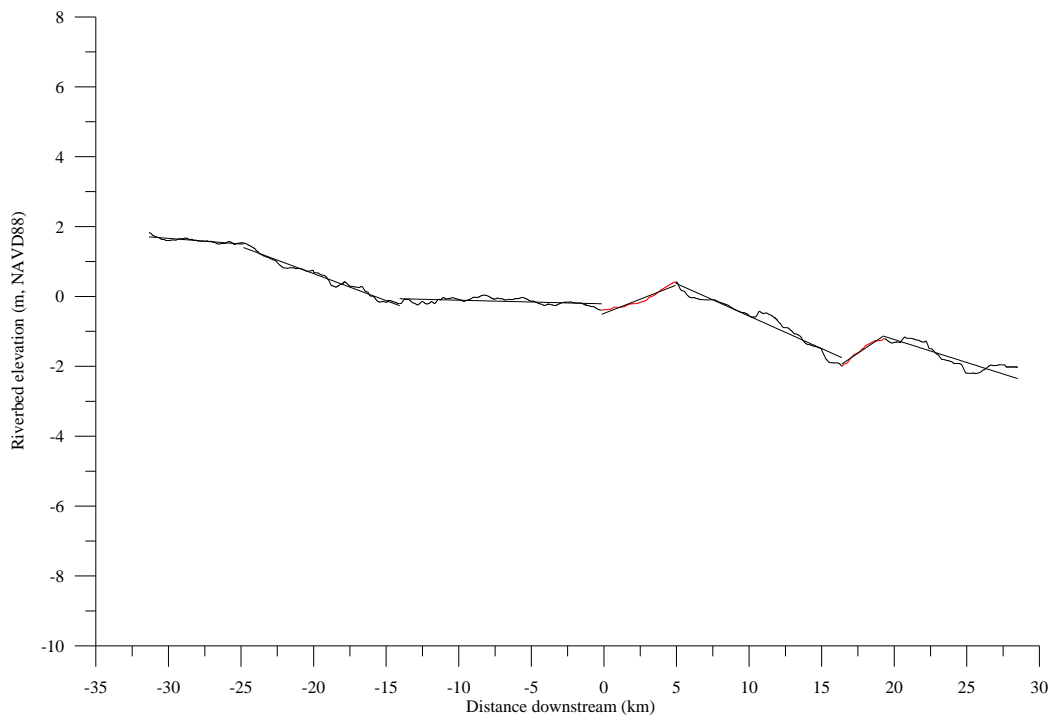
B.1 A 5-km moving averaged riverbed

Figure B.1: A 5-km moving average smoothed riverbed slope. Note that there are seven distinct slopes of the riverbed. Although the entire long profile is characterized by the average slope of -5.74×10^{-5}, the bed profile shows local changes in slope. From upstream, the first three, the fifth and the seventh fit in the downstream exhibit downstream slopes, whereas the fourth and the sixth (denoted red) show upstream slopes.

The riverbed long profile has been smoothed with a 5-km running mean (Figure B.1). The bed profile is divided into seven differently sloped reaches, highlighted by the exponents of the linear fits that vary between –5 and –4. The majority of the slope face downstream, but two slopes trend upstream for ~ 5 km and ~ 3 km as shown in red. The first slope from -35 km to -25 km is $-3.22\text{x}10^{-5}$. The next two, from -25 km to -14 km, and from -14 km to 0 km the bed becomes steeper and then turns gentler at $-1.55\text{x}10^{-4}$ and $-1.04\text{x}10^{-5}$, respectively. From 0 km to +5 km, the slope trends up at $+1.63\text{x}10^{-4}$. From +5 km to +17 km the slope is $-1.86\text{x}10^{-4}$. From +17 km to +19.5 km, it trends up again at $+2.8\text{x}10^{-4}$, and from +19.5 km to +30 km, it descends at $-1.32\text{x}10^{-4}$. The first three trend lines show downstream slopes, but the last four slopes form two local "peaks" by alternating from increasing to decreasing trends in the downstream direction (Figure B.1). It is notable that both increasing and decreasing slopes are at $\pm10^{-4}$. The first upstream slope corresponds to the bedrock section noted in Chapter 2, and both the up-dip sections exhibit low sinuosity.

B.2 Sinuosity (*S*) versus Asymmetry (*a*)

A weak positive relationship exists between sinuosity and asymmetry $2.28\text{x}10^{-1}$ (R^2=0.11) (Figure B.2). About 80% of the asymmetry ranges from 1.1 to 2.1 and occurs at sinuosity <1.25. The seven peak sinuosity values previously noted (Figure 4.3) tend to have asymmetry of >1.4. Therefore, the Santee River's sinuosity versus asymmetry relationship shows higher sinuosity related to higher asymmetry; the more severe the bend the larger contrast between the cut-bank side and the point-bar side, thereby increasing asymmetry.
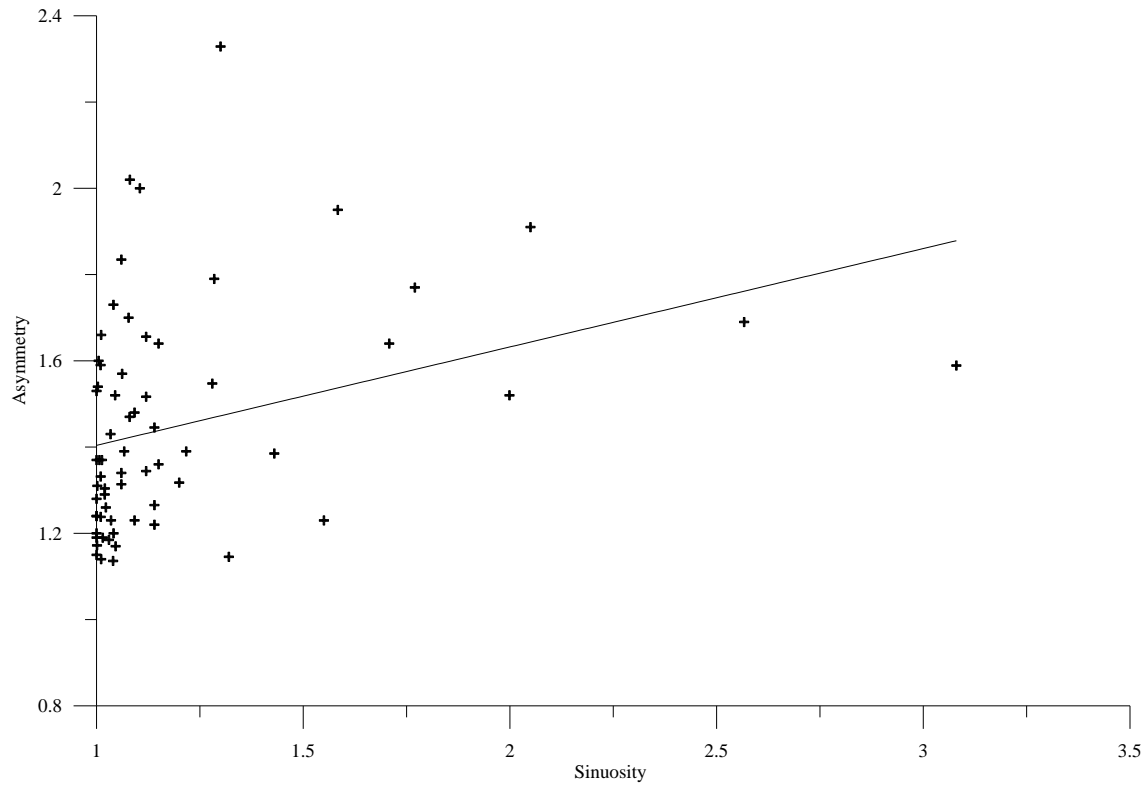
Figure B.2 Sinuosity (*S*) versus asymmetry (*a*). These two parameters exhibit a weak correlation, $22.8x^{-1}$ (R^2=0.22), which links higher sinuosity to higher asymmetrry; at channel bends the cut-bank thalweg side is deeper than the point-bar side.

B.3 Natural log width (*w*), average depth (*D*) and area (*A*).

Natural log transformed width, average depth and area all all >95% confidence interval (Figure B.3). The plot elucidates the distance trends of the dimensions as the major trends are noted as follows. From −35 km to −2 km, *D* and *A* increase, at $-1.79x^{-2}$ (R^2=0.47) and $-1.82x^{-2}$ (R^2=0.30) respectively, while *w* decreases at $-9.44x10^{-4}$ (R^2=0.01). From -2 km to +30 km in the downstream, all three categories decrease: *A* at $-1.46x10^{-2}$ (R^2=0.57), *w* at $-1.94x10^{-2}$ (R^2=0.28) and *D* at $-2.73x10^{-3}$(R^2=0.01). Significantly, the trends start to decline in the downstream after a sudden increase at −2 km.

71

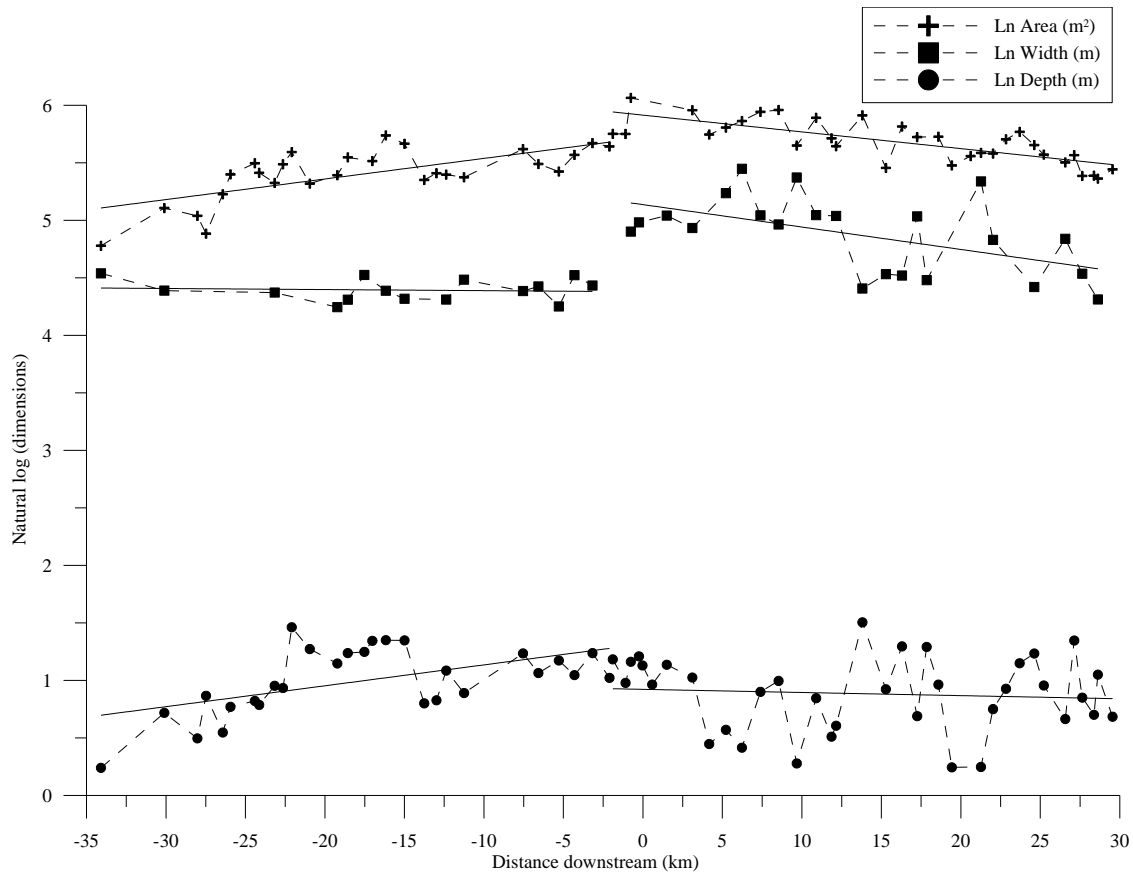Figure B.3 Natural log transformed width, depth and area values (CI >95%) downstream. From –35km to –2km, area and depth increase at -1.79×10^{-2} (R^2=0.47) and -1.82×10^{-2} (R^2=0.30), whereas width decreases at -9.44×10^{-4} (R^2=0.01). From –2 km to +30 km area, width and depth all decrease at -1.46×10^{-2} (R^2=0.57),-1.94×10^{-2} (R^2=0.28) and -2.73×10^{-3}(R^2=0.01), respectively. Note the step-like increase of area and width at −2 km, while depth appears to decrease steadily from −7.5 km to +3 km.

The Levene's test for two variances of the metrics was performed for the apparent upstream (from –35 km to –2 km) and the downstream (from –2 km to +30 km) distinctions of the trends. The *D* trends almost entirely overlapped in a box plot, with a P-value of 0.96. By contrast, the *A* trends had little overlap, having a P-value of 0.25 and thus still lacking statistical significance. The *w* trends, however, had no overlap with a (P-value = 0.00), bolstering the visually recognized trends of *w*.